American Mineralogist, Volume 103, pages 1674–1689, 2018

Changes in physical properties of 4*C* pyrrhotite (Fe_7S_8) across the 32 K Besnus transition

Michael W.R. Volk[1,*], Eric McCalla[2,3], Bryan Voigt[2], Michael Manno[2], Chris Leighton[2], and Joshua M. Feinberg[1]

[1]Institute for Rock Magnetism, Department of Earth Sciences, University of Minnesota, 116 Church Street SE, Minneapolis, Minnesota 55455, U.S.A.
[2]Department of Chemical Engineering and Materials Science, University of Minnesota, 421 Washington Avenue SE, Minneapolis, Minnesota 55455, U.S.A.
[3]Chemistry Department, McGill University, 801 Sherbrooke St. W, Montréal, Québec H3A 0B8, Canada

Abstract

Pyrrhotite, Fe_7S_8, is a common sulfide mineral in the Earth's crust and mantle, as well as in a range of meteorites and is of interest to a wide variety of disciplines including economic geology, geophysics, and material science. The 4*C* variety of pyrrhotite shows a dramatic change in magnetic properties at $T \approx 30$ K, known as the Besnus transition. Although this transition is frequently used to detect pyrrhotite in geologic samples, the underlying mechanism driving the transition has not yet been identified. This study presents a high-resolution view of the changes in heat capacity, magnetic, and electronic properties of a natural single crystal of nearly pure, monoclinic 4*C* pyrrhotite across the Besnus transition. Contrary to previous studies, *all* of these properties show clear evidence of the Besnus transition, specific heat, in particular, revealing a clear transition at 32 K, apparently of second-order nature. Small-angle neutron scattering data are also presented, demonstrating an unusual change in short-range magnetic scattering at the transition. Furthermore, a magnetic field dependence of the transition temperature can be seen in both induced magnetization and electrical resistivity. These new observations help narrow the possible nature of the phase transition, clearly showing that interactions between intergrown coexisting 4*C* and 5*C** superstructures, as suggested in some literature, are not necessary for the Besnus transition. In fact, the changes seen here in both the specific heat and the electronic transport properties are considerably larger than those seen in samples with intergrown superstructures. To further constrain the mechanism underlying the Besnus transition, we identify five separate potential models and evaluate them within the context of existing observations, thereby proposing experimental approaches that may help resolve ongoing ambiguities.

Keywords: Besnus transition, phase transition, magnetism, heat capacity, resistivity, sulfide, pyrrhotite

Introduction

Iron mono-sulfides, or pyrrhotites ($Fe_{1-x}S$, $0 < x < 0.125$), are commonly occurring iron sulfide minerals that are important to a wide range of scientific disciplines. In the Earth and planetary sciences, 4*C* pyrrhotite (Fe_7S_8) acts as a recognizable ferrimagnetic phase and is found in many magmatic and metamorphic rocks (Dunlop and Özdemir 1997), in claystones (Aubourg and Pozzi 2010), and in limestones (Muttoni 1995). In terrestrial rocks, the remanent magnetization carried by this phase has been used to study polarity reversals of the Earth's magnetic field (e.g., Quidelleur et al. 1992) and to examine the nature of magnetization in quartzite clasts from the Precambrian Jack Hills of Western Australia (Weiss et al. 2015), as well as being the basis for a crustal geo-thermometer (Aubourg and Pozzi 2010) or barometer (Gilder et al. 2011). Furthermore, 4*C* pyrrhotite is a major magnetic constituent of several classes of meteorites, most notably in martian meteorites (Rochette et al. 2001). Since pyrrhotite is thermodynamically stable on the surface of Mars, it may also contribute to the martian magnetic anomalies (Fegley et al. 1995). Moreover, 4*C* pyrrhotite can be found in chondritic meteorites, the most primitive and oldest class of meteorites (Herndon et al. 1975; Zhang et al. 2008), and, as such, may possibly record the magnetic fields in the early solar system, as well as transient fields associated with impact events (Muxworthy et al. 2017). In general, pyrrhotites are also the most common iron sulfide minerals in certain intrusions, such as the 1.1 Ga Duluth Complex, which hosts economically important quantities of Cu, Ni, and Pt group elements. Understanding the oxidation kinetics of pyrrhotite minerals in mine tailings is of critical importance for avoiding water quality degradation due to acid mine drainage (Lapakko 2015). Furthermore, pyrrhotite commonly occurs as inclusions in diamonds and may provide information about sulfur cycling within the lower mantle (Sharp 1966; Gilder et al. 2011). Within the material science community, pyrrhotites have been studied as potential candidate materials for anodes in lithium-ion batteries (Zhang et al. 2015) and can be used to sequester arsenic contamination in the environment (Cantu et al. 2016).

Given its importance to geoscience and materials science, the

* E-mail: mvolk@umn.edu

0003-004X/18/0010–1674$05.00/DOI: http://doi.org/10.2138/am-2018-6514

proper characterization of pyrrhotite within natural and synthetic samples is critical, yet frustratingly difficult. As discussed in more detail below, iron monosulfides can display a wide range of crystallographic symmetries and superstructures based on their composition and growth history, and frequently occur as finely intergrown polycrystalline assemblages. Thus, reflected light and electron microscopy methods are often combined with electron and neutron diffraction to properly determine the structure of small iron monosulfide grains. However, magnetic methods are one of the few techniques that allow researchers to characterize the presence of pyrrhotite in bulk samples. In particular, observations of the low-temperature magnetic transition at approximately 30 K (the "Besnus" transition) of 4*C* pyrrhotite have been used with increasing frequency as a diagnostic indicator for the presence of pyrrhotite (Dunlop and Özdemir 1997). Low-temperature superconducting quantum interference device (SQUID) magnetometers are typically sensitive enough to detect 4*C* pyrrhotite in natural samples at parts per million concentrations (Rochette et al. 1990).

Despite the utility of low-temperature magnetic methods in detecting the presence of pyrrhotite in natural and synthetic samples, there is remarkably little consensus on the mechanism that underlies this dramatic change in magnetic properties. The aim of this study is to provide a high-resolution view of the physical (heat capacity and resistivity) and magnetic properties (remanence and high- and low-field induced magnetization) across the Besnus transition in a phase-pure specimen of 4*C* pyrrhotite. Small angle neutron scattering is also presented to help determine the length scales over which the changes in magnetic properties take place. This new data provides the necessary evidence to differentiate between competing models that seek to explain this phenomenon and will enable researchers to more accurately interpret its magnetic recording on Earth and other planetary bodies.

Superstructures

Pyrrhotite occurs in many polytypes that are often intergrown or show incommensurate chemical composition. Similar to troilite (FeS), these polytypes crystallize in a NiAs-like structure with alternating filled and vacant Fe layers oriented parallel to the *a-b* plane containing variably ordered vacancies (Morimoto et al. 1970). Within each Fe-layer the spins are coupled ferromagnetically. However, adjacent layers are coupled antiferromagnetically via superexchange through the S atoms, which in turn forms distorted S octahedra around the Fe atoms (Levinson and Treves 1968). Ordering of the vacancies gives rise to superstructures, which are referred to using an *NC* notation, where *N* gives the number of stacked NiAs cells along the crystallographic *c*-axis. Four commensurate hexagonal varieties, FeS (2*C*), Fe_9S_{10} (5*C*), $Fe_{10}S_{11}$ (11*C*), and $Fe_{11}S_{12}$ (6*C*), and one monoclinic Fe_7S_8 (4*C*) are stable at ambient conditions (Nakazawa and Morimoto 1970; Morimoto et al. 1970). The ordering of the vacancies in hexagonal polytypes creates a zero net magnetization, and thus hexagonal pyrrhotites are non-ferro/ferri-magnetic in the bulk, and incapable of retaining a spontaneous magnetization.

On the other hand, ordering of vacancies in the most Fe deficient variety of pyrrhotite, Fe_7S_8 (4*C*), creates a small lattice distortion ($\beta \neq 90$), which lowers the mineral's symmetry to monoclinic (Powell et al. 2004), and is often referred to as "pseudo-hexagonal." Furthermore, the ordered vacancies in 4*C* pyrrhotite produce a small net magnetization, which gives rise to ferrimagnetism up to its Néel temperature of 598 K (Powell et al. 2004). Within the 4*C* cell, the layers can be labeled as *FAFBFCFD*, where *F* denotes a filled Fe layer and *A–D* are four distinct vacancy layers. Each layer with vacancies contains four unique Fe sites (Bertaut 1953; Tokonami et al. 1972). Of these Fe sites, two have no vacancies above or below, while the Fe atoms in the filled (*F*) layers are adjacent to either one or two vacancies (Ericsson et al. 1994). Superexchange coupling through the S atoms is stronger than the direct Fe-Fe coupling (Levinson and Treves 1968). Consequently, sites that do not have vacancies above or below should be largely unaffected by changes in vacancy ordering (Levinson and Treves 1968).

Phase transition

At T_{Bes} ~30 K, 4*C* pyrrhotite undergoes a magnetic phase transition first described by Besnus and Meyer (1964). The Besnus transition is commonly used to identify pyrrhotite in rocks (Rochette et al. 2011). Similar to the Morin transition in hematite (Fe_2O_3) or the Verwey transition in magnetite (Fe_3O_4), the transition is marked by a loss of remanent magnetization on cooling and a drastic change in fundamental magnetic properties (Fillion and Rochette 1988; Dekkers et al. 1989; Rochette et al. 1990; Dunlop and Özdemir 1997). Furthermore, the anisotropy constants and the direction of the magnetic easy axis change during cooling (Mikami et al. 1959; Bin and Pauthenet 1963; Sato et al. 1964; Rochette et al. 1990). At room temperature, the easy axis lies within the basal (*a-b*) plane of the crystal but this progressively rotates out of the basal plane toward the *c* axis upon cooling below 205 K (Bin and Pauthenet 1963; Powell et al. 2004). While a self-reversal of the magnetization has been observed in very large pyrrhotite crystals (Fillion and Rochette 1988), the direction of the remanence vector at room temperature remains constant upon cycling through T_{Bes} (Feinberg et al. 2015).

While the Besnus transition has been known to our community for more than 50 yr, the mechanism driving the transition is not well understood. Two prevailing explanations exist. Wolfers et al. (2011) measured neutron diffraction and magnetic torque on twinned single crystals. The magnetic torque shows a sixfold symmetry above T_{Bes}, which changes to a fourfold symmetry below the transition. Based on the change in symmetry, Wolfers et al. (2011) propose a crystallographic transition from the monoclinic $F2/d$ ($T > T_{Bes}$) to a triclinic $F\bar{1}$ ($T < T_{Bes}$) structure. This mechanism is similar to the change from cubic to monoclinic symmetry that occurs within magnetite upon cooling through the Verwey transition at $T \approx 110$ K. The second explanation was proposed by Charilaou et al. (2015) and later expanded upon by Koulialias et al. (2016, 2018). Here, the change in magnetic properties is explained by changing magnetic interactions between two different coexisting superstructures (4*C* and 5*C**). The proposed 5*C** phase in Charilaou et al. (2015) possesses a different vacancy ordering, but the same overall chemical composition as the 4*C* structure. Their arguments against a crystallographic phase transition as the basis of the Besnus transition are based in large part on the absence of a transition in the heat capacity $C_P(T)$, and the presence of a second inflection in hysteresis loops

at low temperatures ($T < 200$ K). Clearly, this explanation relies on the existence of two distinct coexisting phases of $Fe_{1-x}S$.

In a previous study, we measured major hysteresis loops in 72 directions within the basal plane of an oriented single crystal of phase-pure 4*C* pyrrhotite (Volk et al. 2016). The chemical composition and crystallographic orientation of the crystal were determined by energy-dispersive X-ray spectroscopy (EDX) and electron backscatter diffraction (EBSD). The experiments were conducted at 21 temperatures spanning the Besnus transition (20–50 K). Several magnetic properties showed a sixfold symmetry above T_{Bes}, including the second hysteresis inflection described by Koulialias et al. (2016). However, we found that these magnetic symmetries change from sixfold ($T > T_{Bes}$) to fourfold ($T < T_{Bes}$), consistent with the behavior originally observed by Wolfers et al. (2011). Furthermore, the second hysteresis inflection disappeared below T_{Bes}. To better differentiate between the competing models, we present here a detailed study of the structural, magnetic, and electronic properties of a second Fe_7S_8 single crystal subsampled from the same piece used in Volk et al. (2016) from Morro Velho, Brazil, provided by the Munich Mineralogical State Collection (Mineralogische Staatssammlung München).

Results and discussion

The chemical composition of the sample was determined by electron microprobe analysis with a JEOL JXA-8900R operated with a beam energy of 20 keV, a current of 20 nA, and diameter of 5 μm. Detection limits ranged from 0.020 wt% for Fe*K*α to 0.022 wt% for S*K*α and analytical sensitivity (at the 99% confidence level) ranged from 0.157% relative for Fe*K*α to 0.406% relative for S*K*α. Elements were acquired using analyzing crystals LiFH for Fe*K*α, and PETJ for S*K*α. The standards were Fe for Fe*K*α, and pyrite FeS_2 for S*K*α. The specimen's bulk chemical composition, determined from 12 measurements, is $Fe_{6.78\pm0.12}S_8$ ($Fe_{0.85}S$, Fe = 45.9 at%). According to the phase diagram of Nakazawa and Morimoto (1970), the sample's measured composition is within in the stability field of 4*C* pyrrhotite. Significantly, no impurities, such as Ni, were detected in any of the 12 measurements (within the limits stated above).

In naturally occurring rocks, pyrrhotites are often an intergrown mixture of both the hexagonal and monoclinic phases (Arnold 1967). In our case, it is particularly important to detect the presence of any such hexagonal intergrowths, since one of the proposed mechanisms for the Besnus transition requires the presence of both 4*C* and 5*C** superstructures (Charilaou et al. 2015; Koulialias et al. 2016). Non-magnetic hexagonal phases transform into a ferrimagnetic phase between 200–265 °C depending on their iron content (Schwarz and Vaughan 1972). This transformation, due to a rearrangement of vacancies, is identified as a sudden rise in magnetic susceptibility, known as the λ-transition (Schwarz and Vaughan 1972). We measured magnetic susceptibility as a function of temperature using a Geophysica Kappabridge KLY-2 (300 Am^{-1} field at 920 Hz), which is able to detect even small hexagonal impurities. The specimen shows a single Néel temperature (318 °C, 591 K) close to the literature value [320 °C (Dunlop and Özdemir 1997)] with no sign of a λ-transition, as shown in Supplemental[1] Figure S1. This conclusion of the absence of any significant amount of 5*C** phase is further supported by structure determinations, also, as discussed below.

Powder X-ray diffraction

To detect possible inclusions (e.g., pyrite FeS_2) in our pyrrhotite sample, or pyrrhotite polytypes (e.g., the 5*C** phase discussed above), room temperature powder X-ray diffraction (PXRD) data were acquired with a PANalytical X'Pert PRO X-ray diffractometer equipped with a Co source (0.17909 nm) and an X'Celerator detector. The diffraction patterns were collected from 10–90° scattering angle in 0.0167° steps with an effective dwell time of 100 s per step.

Figure 1 shows the PXRD pattern along with the result of Rietveld refinement with a single phase with a 4*C* stacking sequence. The software Rietica was used to fit the data using the structural model by Powell et al. (2004). The fitted cell parameters of the monoclinic space group *C*2/*c* are $a = 1.1915(1)$ nm, $b = 0.68698(6)$ nm, $c = 1.2907(1)$ nm, and $\beta = 118.005(1)°$, with quality parameters of $R_{Bragg} = 2.87\%$, $R_P = 2.24\%$, and $R_{WP} = 3.51\%$. The lattice parameters agree well with the values for the 4*C* phase obtained by Charilaou et al. (2015). Furthermore, the composition obtained by PXRD refinement is $Fe_{6.76}S_8$ ($Fe_{0.83}S$), in excellent agreement with the measured chemical composition from electron microprobe analysis. The PXRD results thus indicate that the crystal is pure monoclinic 4*C* pyrrhotite without any detectable contamination from other minerals (e.g., oxides) or vacancy superstructures. It is important to note that the hexagonal (5*C**) phase, which is clearly present in the PXRD data presented by Charilaou et al. (2015) (see Fig. 1 inset), is not present here, within the limits of detection.

Small-angle neutron scattering

Small-angle neutron scattering (SANS) from a 4*C* pyrrhotite single crystal was used to investigate potential structural and/or magnetic changes across the Besnus transition. This powerful method (Muhlbauer et al. in review[2]), which has not yet been applied to pyrrhotite, provides length-scale-dependent information on structural and magnetic inhomogeneities across a wide range. In essence, the neutron scattering cross-section, $d\Sigma/d\Omega$, is measured as a function of the scattering wavevector, Q, revealing information on a length scale $2\pi/Q$. Importantly, in the unpolarized case used here, the inhomogeneities that generate the scattering can be structural (e.g., long-range defects, twins, twin boundaries) or magnetic (e.g., domains and domain walls, short-range magnetic fluctuations, etc.). The SANS measurements presented were taken on the NG7 30 m SANS beamline at the NIST Center for Neutron Research, at six temperatures between 5 and 60 K, i.e., around the Besnus transition. At each temperature, 2D area scans, or Q_x-Q_y intensity maps (see Fig. 2a), were collected in two frames (one at $0.004 < Q < 0.025$ $Å^{-1}$ and one at $0.02 < Q < 0.15$ $Å^{-1}$), resulting in a total covered Q range from 0.004 to 0.15 $Å^{-1}$. We thus probe real-space length scales ($2\pi/Q$) from 4 to 160 nm. In such scans, the incoming neutron beam is perpendicular to the plane of the detector, the dark region in the center of Figure 2a is a beam-stop covering the unscattered beam, and displacement outward from the origin corresponds to increasing Q.

Figure 2 shows the SANS results obtained with a sister

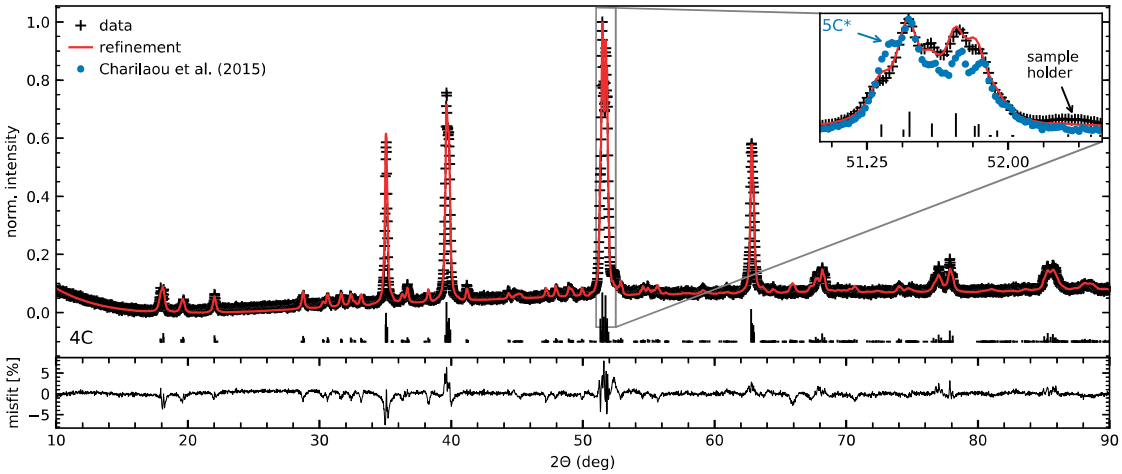

FIGURE 1. Powder X-ray diffraction (room-temperature) of a sister specimen using Co radiation. The red line shows the fit obtained with Rietveld refinement. The inset shows an expanded view of the most prominent peak, in comparison with data from Charilaou et al. (2015) in blue. The misfit is between the refinement and data.

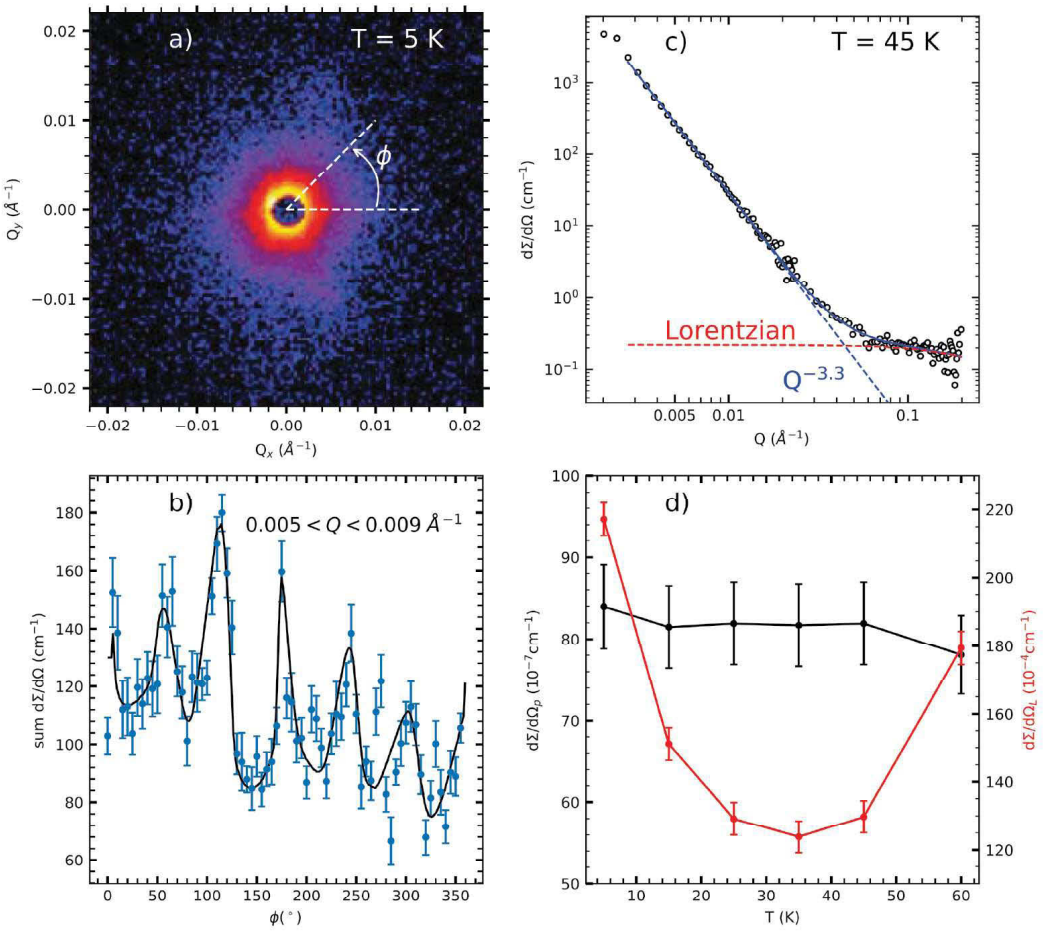

FIGURE 2. SANS results obtained with a 4*C* pyrrhotite crystal. (**a**) The low-Q 2D scattering pattern (Q_x-Q_y map) obtained at 5 K (the brightness/color of each pixel indicates the differential scattering cross section). (**b**) The sum of scattering cross sections over the indicated low-Q range ($0.005 < Q < 0.009$ Å^{-1}) as a function of the in-plane angle, ϕ, as defined in panel **a**. These data were averaged over all six temperatures probed (from 60 to 5 K), due to the absence of any significant temperature dependence of the angular dependence. (**c**) A representative ($T = 45$ K) scattering cross section ($d\Sigma/d\Omega$) vs. Q scan obtained by circular integration of the 2D scattering patterns. The fit (solid blue line) is the sum of a Porod term (blue dashed line) and a Lorentzian term (red dashed line), as discussed in the text. These two terms are defined by $d\Sigma/d\Omega = (d\Sigma/d\Omega)_P/Q^n + (d\Sigma/d\Omega)_L/(Q^2 + \kappa^2)$, where "P" and "L" subscripts are for Porod and Lorentzian, n is the generalized Porod exponent, and κ is defined in the text. (**d**) The temperature (T) dependence of the Porod (black) and Lorentzian (red) cross sections.

specimen to the main crystal studied in this work, oriented with the *c*-axis approximately parallel to the neutron beam. Figure 2a shows an example 2D area scan (i.e., a Q_x-Q_y intensity map), at 5 K, out to Q_x/Q_y values of 0.02 Å^{-1}, i.e., probing real space length scales above 30 nm. The sixfold in-plane symmetry is obvious in the 2D scan, and, due to the use of unpolarized neutrons, could arise from structural effects (such as long-range (>30 nm) defects aligned with high-symmetry in-plane directions) or from magnetic domain formation along specific axes (note that the data were recorded here after nominal zero field cooling). Of high interest in terms of the aforementioned potential explanations for the Besnus transition, the observed sixfold pattern *did not* alter significantly across the 32 K transition temperature. The angular scan in Figure 2b, which simply shows the cross section summed over the small range $0.005 < Q < 0.009$ Å^{-1} (to improve statistics), was in fact averaged over all temperatures between 5 and 60 K, no significant changes in the angular dependence occurring at any *T*. Sixfold periodicity is thus clear, but, remarkably, it is not *T*-dependent across the Besnus transition. If a crystal symmetry change occurs at 32 K, this indicates that the long-range (>30 nm) structural defects or magnetic domains producing the scattering seen here do not change significantly in response.

There are, however, some subtle changes in the absolute scattering intensity. To illustrate this, Figure 2c plots $d\Sigma/d\Omega$ vs. the magnitude of *Q*, acquired by circular averaging of 2D maps of the type shown in Figure 2a; the example shown here is at 45 K. As is often the case, $d\Sigma/d\Omega(Q)$ can be fit (solid line through the points) as the sum of two terms: A Porod term (blue dashed line) and a Lorentzian term (red dashed line). The generalized Porod term has the form $d\Sigma/d\Omega = (d\Sigma/d\Omega)_P/Q^n$, where the exponent *n* provides details on the morphology of the scattering inhomogeneities, and the prefactor $(d\Sigma/d\Omega)_P$ parameterizes the strength of the Porod intensity. In our case $n = 3.3$ (i.e., somewhat less than 4), as shown in Figure 2c, indicating that the scattering inhomogeneities (long-range structural defects or magnetic domains) do not have completely smooth surfaces. A value of 3.3, however, not far from the generic 4.0 for smooth 3D objects, indicates that the scattering is *not* occurring from clearly one- or two-dimensional objects, such as filaments or lamellae. The Lorentzian term has the form $d\Sigma/d\Omega = (d\Sigma/d\Omega)_L/(Q^2 + \kappa^2)$, where the prefactor $(d\Sigma/d\Omega)_L$ parameterizes the strength of the Lorentzian intensity, and κ is a constant. Such scattering is most commonly associated with short-range (nanometer-scale) magnetic fluctuations, where κ becomes $1/\xi$, the magnetic correlation length. Standard behavior in a ferrimagnet would involve an order-parameter-like turn on of the Porod scattering from magnetic domains below the magnetic ordering temperature, along with a peak in Lorentzian scattering at the ordering temperature due to critical scattering. At $T \leq 60$ K, far below the ordering temperature, Lorentzian scattering should thus be small, and, if present at all, be decreasing on cooling. Not only does Figure 2c show that the Lorentzian scattering here is non-negligible, but Figure 2d shows that it has an unusual *T* dependence. Specifically, $(d\Sigma/d\Omega)_L$ (right axis, red points) decreases on cooling from 60 to 35 K, as might be expected, but then *grows* on further cooling to 5 K. This is unusual in a long-range-ordered ferro- or ferri-magnet far below its ordering temperature. The Besnus transition thus manifests itself in some change in short-range (<10 nm) spin fluctuations/ordering in 4*C* pyrrhotite, but not obviously so in the angular dependence of long-range (>30 nm) scattering. We note that the *T* dependence of $(d\Sigma/d\Omega)_P$ (left axis, black points in Fig. 2d) may provide some evidence of a plateau around the Besnus transition, although much better statistics would be required to reinforce this. Future SANS measurements to probe these findings in more detail could employ a much wider *T* range (going above the Néel temperature) or polarized neutrons to better separate magnetic and structural scattering. Both of these approaches are certainly possible.

Heat capacity

As discussed above in the Introduction, the existence of an anomaly in specific heat capacity (C_P) at the Besnus transition is important in pyrrhotite but is not clear from prior experimental work. Specifically, the work of Grønvold et al. (1959) indicated a small anomaly around 32 K, while the work on material with mixed 4*C*/5*C** superstructures by Charilaou et al. (2015) revealed no such anomaly. In general, first-order phase transitions involve latent heat and result in discontinuities in $C_P(T)$, while second-order transitions involve no latent heat and result in peaks in $C_P(T)$. To probe these issues in our 4*C* pyrrhotite single crystal, $C_P(T)$ was measured in a Physical Property Measurement System (PPMS) from Quantum Design Inc., from 1.8 K to room temperature. Relaxation calorimetry was employed, using temperature pulses amounting to 2% of the sample temperature. The crystal was attached to the measurement platform using Apiezon N grease, and the heat capacity of the platform and grease were subsequently subtracted. For all measurements, the ratio of sample to addenda heat capacity was maintained at greater than 2.0, safely above the recommended minimum of 0.5 from Lashley et al. (2003). Similarly, the thermal coupling parameter between the sample and calorimeter was >96%, well above the minimum Quantum Design recommendation of 90%.

Figure 3 shows our $C_P(T)$ results along with those obtained from Grønvold et al. (1959), Kobayashi et al. (1999), and Charilaou et al. (2015). Figure 3a shows $C_P(T)$ over the entire *T* range studied (1.8–300 K), generally showing good agreement with previous studies over most of the *T* range. Around the Besnus transition, however (inset to Fig. 3a), the results are substantially different in the various studies. In our work, $C_P(T)$ exhibits a large anomaly at 31.7 K, larger than the one seen by Grønvold et al. (1959) (in a synthetic sample), and in contrast to the lack of any anomaly seen by Charilaou et al. (2015). In the latter work, multiple stacking sequences (i.e., coexisting 4*C* and 5*C** phases) were clearly observed in XRD. Here, however, we have a phase-pure 4*C* pyrrhotite crystal, which apparently results in a clear, well-defined transition in $C_P(T)$, taking the form of a classic "λ anomaly" expected at a second-order phase transition. (Note that this is not to be confused with the 220 °C "λ-transition" in hexagonal pyrrhotite, as discussed above.) The apparent second-order nature of the transition is supported by the absence of any detectable thermal hysteresis, both in relaxation calorimetry on cooling and warming and by the use of long-pulse measurements (Gillard et al. 2015). The striking differences between our phase-pure 4*C* natural single crystal and the 4*C*/5*C**

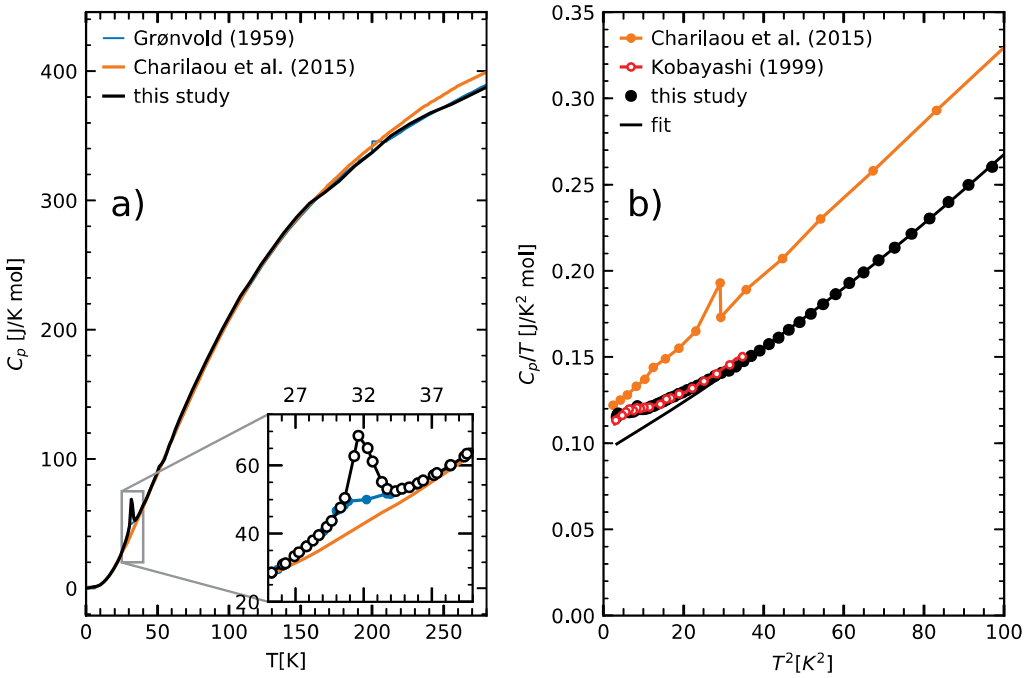

FIGURE 3. Heat capacity measurements obtained in this study along with those from previously published studies. (**a**) C_P as a function of temperature (T), with the inset focusing on the Besnus transition at 32 K. The solid lines are simple linear segments connecting data points. (**b**) C_P/T as a function of T^2 at low temperature. The solid black line is a fit to the data as described in the text.

natural crystal of Charilaou et al. (2015) may well result from the phase-purity with respect to the stacking sequences, and/or trace concentrations of other metals (particularly nickel). It is interesting to note that the 5*C* polymorph measured later by Grønvold et al. (1991) (not shown in Fig. 3) also shows no $C_P(T)$ anomaly, suggesting that the pure 4*C* structure may be the only form of pyrrhotite that displays a heat capacity anomaly at the Besnus transition, and that any changes in properties across the Besnus transition are intrinsic to 4*C* pyrrhotite.

Subtracting a linear T-dependent background from our $C_P(T)$ data around the Besnus transition and then integrating the excess specific heat yields the entropy change across the Besnus transition. This gives 2.39 J/(mol·K), or, by mole of Fe, 0.34 J/(mol·K). For comparison, the entropy change across the Verwey transition of magnetite, a first-order structural transition, is approximately 5 J/(mol·K), or by mole of Fe, 1.33 J/(mol·K) (Shepherd et al. 1991). Furthermore, the Morin transition of hematite, a first-order spin-flop transition, has an entropy change of 0.43 J/(mol·K), or, per mole of Fe, 0.22 J/(mol·K) (Pastor et al. 2012). The entropy change across the Besnus transition in 4*C* pyrrhotite is thus significant.

Further analysis was performed on the low-temperature specific heat (Fig. 3b), which can be used to extract electronic and lattice contributions, in turn allowing for determination of the density-of-states at the Fermi level and the Debye temperature, respectively (as discussed later in this work, pyrrhotite is an electronic conductor). As shown in Figure 3b, our $C_P(T)$ in this region is in excellent agreement with that of Kobayashi et al. (1999), but again different to the mixed phase 4*C*/5*C** crystal of Charilaou et al. (2015). Our data were fit following the standard procedure, using $C_P(T) = \gamma T + \beta T^3 + \alpha T^5$, where the first term is the electronic contribution and the latter two are from lattice dynamics. The T^3 term is the standard low-temperature expansion in the Debye model, while the T^5 term is the next-order term, as often needed to adequately describe experimental data. Two fitting procedures were employed, the first considering all data up to 10 K, comparable to that used by Kobayashi et al. (1999). This resulted in a poor fit, with an unphysically large αT^5 term. The second fitting approach acknowledges the clear upturn in the data at $T^2 < 30$ K^2, and fits only at $T^2 > 30$ K^2, resulting in the good fit shown in Figure 3b. Considering the electronic contribution first, the results give $\gamma = 95$ mJ/(mol·K^2), a substantial value. Theoretical values from the density-of-states at the Fermi level calculated from density functional theory suggest ~46.5 mJ/(mol·K^2), however (Shirai et al.1996; Shimada, et al. 1998), corresponding to only a modest effective mass enhancement of ~2, in good agreement with Shimada et al. (1998) and Kobayashi et al. (1999). With respect to lattice contributions, the extracted β was used to determine the Debye temperature, Θ_D, yielding 278 K. This is in reasonable agreement with the value of Kobayashi et al. (1999) ($\Theta_D = 313$ K), who, we note, did not include the higher order αT^5 term used here. We add that in our case the αT^5 term is indeed almost an order of magnitude smaller than the βT^3 term, even at the highest T, as would be expected. Finally, with respect to the excess specific heat at $T^2 < 30$ K^2 [i.e., below 5.5 K, as also seen in Kobayashi et al. (1999)] we note only that upturns on $C_P(T)$ vs. T^2 plots at the lowest T are not at all uncommon in solid-state systems and can derive from Schottky anomalies, (for example, see Rosenberg 1963; Gopal 1966). The latter occurs due to any mechanism that produces a manifold of low-lying states and can result from all manner of origins; further study at temperatures well below 1 K could clarify this.

Magnetic properties

Remanent and induced magnetization. In paleomagnetism, the Besnus transition is associated with a loss in remanent magnetization on cooling. We measured the temperature dependence of a room-temperature saturation isothermal magnetization (RTSIRM) with a quantum design magnetic property measurement system (MPMS-XL) on cooling and warming. The specimen acquired a RTSIRM in a 2.5 T magnetic field at 300 K applied along two arbitrarily chosen directions in the basal plane of the crystal (Φ_1, Φ_2), both roughly perpendicular to the [001] *c*-axis. The temperature dependence of the RTSIRM was measured twice, first spanning the full temperature range from 300–10 K (5 K/min) and second in high resolution (0.5 K/min) spanning the transition (20–50 K).

The cooling path (Fig. 4 insets) of the RTSIRM ($\Phi_1 = 1.5$, $\Phi_2 = 1.9$ Am^2/kg) shows a gradual decrease in magnetization to ~45% at 110–150 K, where it plateaus. Characteristic of the Besnus transition (Dekkers et al. 1989), the remanence drops sharply in the narrow temperature range of 35–25 K (Fig. 4). Estimates of the transition from the maximum dM/dT, yield a slightly higher temperature (34 K) than the peak in specific heat (31.7 K). While the shapes of the cooling paths in Φ_1 and Φ_2 are comparable, the warming paths (path 4 in Figs. 4a and 4b) are quite different in the vicinity of T_{Bes}, when measured in high-resolution (0.5 K steps). The recovery of magnetization by warming back through the Besnus transition is strongly dependent on the grain-size of the sample and should be low for large grains (Dekkers et al. 1989). Along Φ_1 (Fig. 4a) a small portion (~5%) of the RTSIRM is recovered on warming from 10 K back to 40 K. In contrast, the measurement along direction Φ_2 (Fig. 4b) shows a zigzag behavior at T_{Bes}, with a local minimum centered exactly at the specific heat peak. Furthermore, Φ_2 shows little remanence recovery. Finally, the remaining remanence decays further with warming and only 20 ± 4% of the initial RTSIRM remains at room temperature.

Dekkers et al. (1989) showed that cycling to 4.2 K changes the median destructive field (MDF) of the sample. Similarly, the second high-resolution cooling/warming cycle (paths 3 and 4) shows that the newly acquired RTSIRM(50 K) is slightly larger than the first one. This indicates that the changes occurring across the Besnus transition may not be entirely reversible. Furthermore, the changes in MDF are grain-size dependent (Dekkers et al.1989), with the biggest increases occurring in larger particles. Thus, the configuration of domain walls in large, multi-domain grains may be altered after cycling through the Besnus transition. A possible rearrangement of vacancies at the transition could change the defect structure of the crystal and lead to different pinning of domain walls and consequently a hardening of MDF and increased remanence ratio (Table 1).

The application of DC magnetic fields can modify the precise temperature of some magnetic transitions, or even influence crystallographic changes during transitions in magnetic materials. For example, in magnetite the orientation of the monoclinic *c*-axis below the Verwey transition can be strongly controlled by the application of a DC magnetic field during cooling, where the monoclinic *c*-axis is selected from the cubic *a*-axis that is closest to the orientation of the applied field (Li 1932; Kasama et al. 2010).

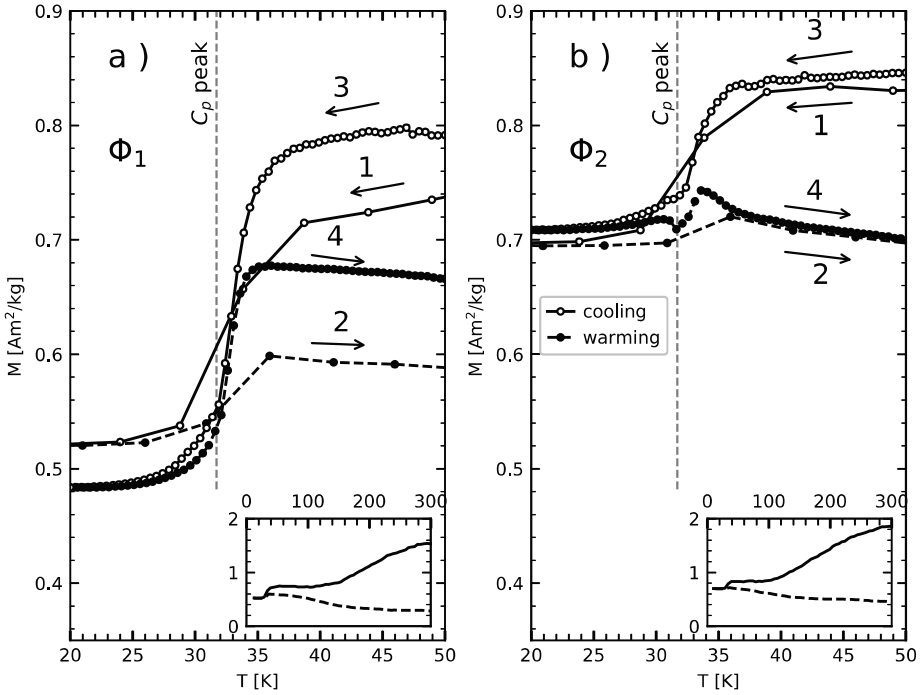

FIGURE 4. Zero field low-temperature cycling of a room-temperature SIRM moment acquired in a 2.5 T field in the basal (**a**–**b**) plane. Parts **a** and **b** show different orientations of the single crystal. The experiment was repeated twice for each orientation, where the first experiment was measured using a larger temperature interval (every 5 K) than the second experiment (every 0.5 K). The magnetization in the second experiment is usually higher than in the first, suggesting a slight hardening after the first thermal cycling. Arrows show cooling or warming, numbers indicate the measurement sequence. Dashed lines denote the temperature of the heat capacity peak. Insets in both **a** and **b** are SIRM moments over the entire temperature range measured, with solid lines being the cooling paths and dashed lines warming.

To look for field-dependent effects at the Besnus transition, we performed in-field cooling (FC) (5 K/min) in 0.5, 1, 1.5, 2, and 3 T (B⊥[001]) followed by zero-field warming (5 K/min) of the low-temperature remanence (LTSIRM) that was acquired in the respective field at 10 K (Fig. 5). The saturation magnetization determined from field cooling [M(300 K, 3 T) = 20.2 Am^2/kg, see Table 1] is well within the range of reported values (18.3–21.2 Am^2/kg) (O'Reilly et al. 2000; Kind et al. 2013). As the sample cools in a field (Fig. 5a), the magnetization increases to a local maximum at $T \approx 180$ K [M(180 K, 3 T) = 21.7 Am^2/kg]. The maximum is located close to where the magnetic anisotropy constant K_4 is also at a maximum and where K_3 changes sign from positive to negative (Bin and Pauthenet 1963).

Cooling in fields lower than ~1.5 T causes a sharp increase of magnetization at the Besnus transition. By comparison, in strong fields (B > 1.5 T), the Besnus transition is only visible as a slight bump in the magnetization, which has been reported in several studies (Besnus and Meyer 1964; Dekkers et al. 1989; Kind et al. 2013; Charilaou et al. 2015; Koulialias et al. 2016). The changing crystalline anisotropy causes the spins, which are lying in the basal plane at room temperature, to rotate out of the plane with decreasing temperature (Bin and Pauthenet 1963; Powell et al. 2004). Thus, the increase in magnetization could be related to a change in spin configuration at the transition.

We can compare the directional dependence of the magnetization with data from magnetic hysteresis loops (Volk et al. 2016), which were measured as a function of orientation (Φ) and temperature on a single-crystal sister specimen from the same sample studied here. Consequently, each magnetization value can be expressed as a function of field, orientation, and temperature M (B, T, Φ) and used to determine quasi "FC" measurement. Figure 5b shows the magnetization in a 500 mT field in different crystallographic orientations as a function of temperature. Similar to the MPMS measurements along Φ_1 and Φ_2 (Fig. 5a), the quasi FC data shows orientation-dependent magnetization. However, these measurements show a clear directional dependence of the shape and magnitude of the Besnus transition. Moreover, the standard deviation of the induced moment is about 2.6 times greater for T =50 K than for T =20 K. The decrease in variability at lower temperature suggests changes in magneto-crystalline anisotropy as the crystal is cooled through the transition.

To check for possible thermal hysteresis, we repeated the FC experiment (500 mT, Φ_2) at a higher resolution (0.5 K). While hysteretic behavior is typical for first-order transitions, no such behavior is expected for second-order ones, as noted above. The fact that both cooling and warming curves are perfectly aligned, completely reversible, and show no hysteresis (inset in Fig. 5b), further underlines the second-order character of the Besnus transition, consistent with our specific heat data.

The remanence acquired in the field-cooling experiments at 10 K (LTSIRM, Fig. 5c) was measured on warming back to room temperature in zero field. The absolute magnetization is the same for all fields used, which drops by 90% at T_{Bes} and further decays to only ~2% at room temperature. While the LTSIRM is about 7 times stronger than the RTSIRM (Table 1) at low temperature, the two are comparable after a full cooling-warming circle. There was no field dependence observed in the warming of LTSIRM for pure 4C pyrrhotite.

TABLE 1. Mean saturation magnetization [$M_s(\theta_1,\theta_2)$] determined from in-field cooling in a 3 T field and saturation remanence (M_{rs}) at 10 (LTSIRM) and 300 K (RTSIRM)

	M_{rs} (Am^2/kg)	M_s (Am^2/kg)	M_{rs}/M_s
10 K	13.85	20.09	0.69
300 K	1.67	20.19	0.08

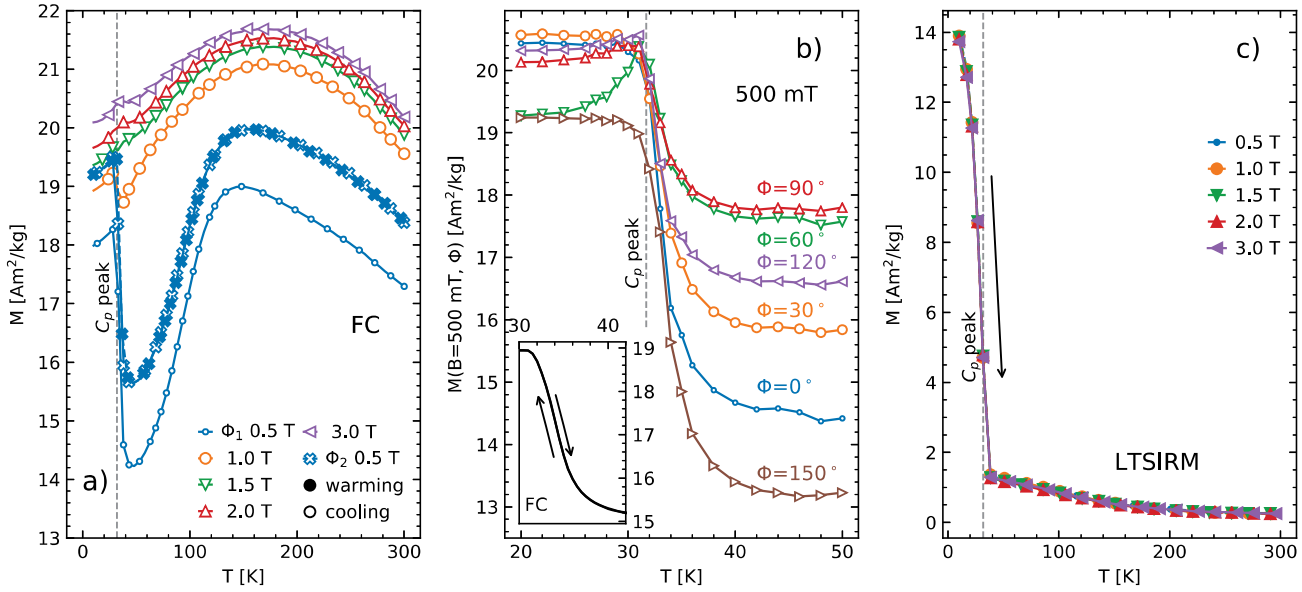

FIGURE 5. Field cooling (FC) experiments in different fields. (**a**) FC in 500 mT was measured along two arbitrary, perpendicular directions in the basal plane (Φ_1, Φ_2). Crosses mark direction Φ_2 on cooling and warming (filled marker). (**b**) shows M(B = 500 mT, T, Φ) determined from hysteresis loops (see text) at selected orientations within the basal plane of an oriented single crystal of Fe_7S_8. Inset in **b** demonstrates the lack of hysteresis of a high-resolution (0.5 K) FC measurement (see **a**) in a 500 mT field (Φ_1) on warming and cooling. (**c**) shows warming of a low-temperature SIRM acquired by cooling in field (**a**) to 10 K.

The $M(B,T,\Phi)$ data (Fig. 5b) from the hysteresis loops, as described earlier, allow for the extraction of T_{Bes} as a function of Φ (in the basal plane) and applied field. We define T_{Bes} (B,Φ) as the maximum change in magnetization [max(dM/dT)] on cooling. T_{Bes} (B,Φ) is determined from a cubic spline interpolation of the smoothed data. Figure 6a shows that the mean $T_{Bes}(\Phi)$ is field dependent, and increases from ~30 to ~34 K as applied field increases from 0 to 1 T. The most prominent change is visible in the first 100 mT (see inset in Fig. 6a), where T_{Bes} changes by ≈2 K from 30 to 32 K. As the field is further increased, T_{Bes} rises linearly until it saturates at 750 mT and 34 K. In our previous study (Volk et al. 2016), we were not able to explain how the coercivity of remanence (B_{cr}) of the single crystal could be lower than its coercivity (B_c) for temperatures <30 K. However, the field dependence of the transition can explain this phenomenon. When B_{cr} is measured in zero field, the crystal is above T_{Bes} and, consequently, the coercivity of remanence is low. B_c, on the other hand, is measured *in* a magnetic field, which raises T_{Bes}. The measurement is therefore done below the transition temperature. B_c is greatly enhanced for $T < T_{Bes}$ that leads to the unusual $B_{cr} < B_c$. Furthermore, the mean $T_{Bes}(B)$ shows a directional dependence (Fig. 6b). Parallel to the crystallographic *a*-axes [determined using EBSD (see Volk et al. 2016)], we find the maximum T_{Bes}, while minima lie between axes, coinciding with orientations whose hysteresis loops most strongly show a second inflection. Finally, combining the field and directional dependence (Fig. 6c) shows the minimum (dark color) of T_{Bes} (30.1 K) located close to the projection of the *c*-axis onto the basal plane with a transition temperature close to the peak in heat capacity. Thus, the highest Besnus transition temperatures occur when a field is applied parallel to one of the *a*-axis directions, while the lowest T_{Bes} occurs in between these directions and closest to the projection of the *c*-axis. It appears as though the application of DC magnetic fields in between the *a*-axes, or even potentially along the *c*-axis, stabilizes the $T >$ T_{Bes} phase, requiring lower temperatures to ultimately bring about the Besnus transition.

Alternating current susceptibility. Measurements of low-field AC susceptibility as a function of temperature can provide important information about the mobility of domain walls as a mineral's intrinsic magnetic anisotropy changes, as the pinning energies of vacancies change, or as a mineral undergoes a crystallographic transition. Low field in-phase (χ') and out of phase (χ'') AC susceptibility between 10 and 300 K (see Table 2) was collected at 5 field amplitudes (0.02–0.3 mT, 5 K/min) on cooling and subsequent warming along the sample's [001] axis ($\chi_{||}$) as well as perpendicular to it ($\chi_{\perp}$, Φ_2). The AC susceptibility (Fig. 7) in the basal plane ($\chi_{\perp}$) shows a gradual decline during cooling until it drops sharply at ~34 K. There is a strong amplitude dependence in both the in-phase (Fig. 7a) and the out-of-phase components (Fig. 7b) of $\chi_{\perp}$. While the amplitude dependence of $\chi_{\perp}$ is approximately constant down to 35 K, it increases dramatically at T_{Bes} and then drops to close to zero below the transition. The measurement of $\chi_{||}$, on the other hand, shows a vastly different behavior. Here, both $\chi_{||}$ and its amplitude dependence decrease with increasing temperature. The maximum of $\chi_{||}$ [17–24 × $\chi_{||}(T_R)$] is reached close to the Besnus transition. Similar to $\chi_{\perp}$, $\chi_{||}$ evidences a sharp change at T_{Bes}. While the measurements in this study come from a multidomain single crystal, Kind et al. (2013) measured

Table 2. Amplitude dependence of susceptibility above (300 K) and below (20 K) T_{Bes}

Amplitude in mT	0.2	0.5	1.0	2.0	3.0
$\chi_{||}$ (300 K)	1.55	1.68	1.82	2.04	2.15
$\chi_{||}$ (20 K)	0.97	0.97	0.95	0.96	0.96
$\chi_{||}$ (20 K/300 K) (%)	62.26	57.72	52.09	47.22	44.74
$\chi_{\perp}$ (300 K)	258.96	296.64	324.94	354.51	370.13
$\chi_{\perp}$ (20 K)	1.84	1.82	1.84	1.83	1.83
$\chi_{\perp}$ (20 K/300 K) (%)	0.71	0.61	0.57	0.52	0.50
$\chi_{\perp}/\chi_{||}$ (300 K)	166.86	176.60	178.43	174.15	172.55
$\chi_{\perp}/\chi_{||}$ (20 K)	1.91	1.87	1.94	1.91	1.91

Note: Absolute values of the susceptibility are given in mAm^{2}kg^{-1}mT^{-1}.

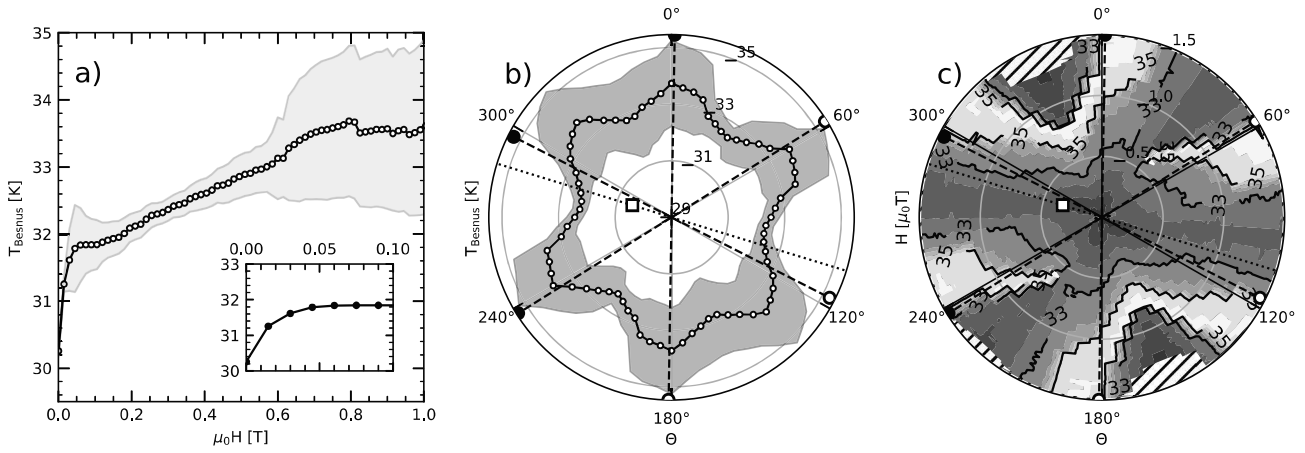

Figure 6. Transition temperature calculated from the maximum of dM/dT of the positive ascending branch of the hysteresis loop for all orientations and fields. (**a**) Average transition temperature with one standard deviation (shaded region) for all orientations as a function of magnetic field. The inset shows a zoomed-in view of the first 100 mT. (**b**) Directional dependence of the mean transition temperature over all applied fields. A data point's distance from the center of the plot corresponds to the T_{Bes} for that orientation and varies between 29 and 35 K. The shaded region shows 1σ uncertainty. (**c**) Contour plot for all fields (radius) and orientation (angle), dark = low, light = high-transition temperature. Hashed regions show the area where T_{Bes} could not be calculated. Dashed lines in **b** and **c** show the crystallographic axis as determined by EBSD. The dotted line is the projection of the c-axis onto the plane.

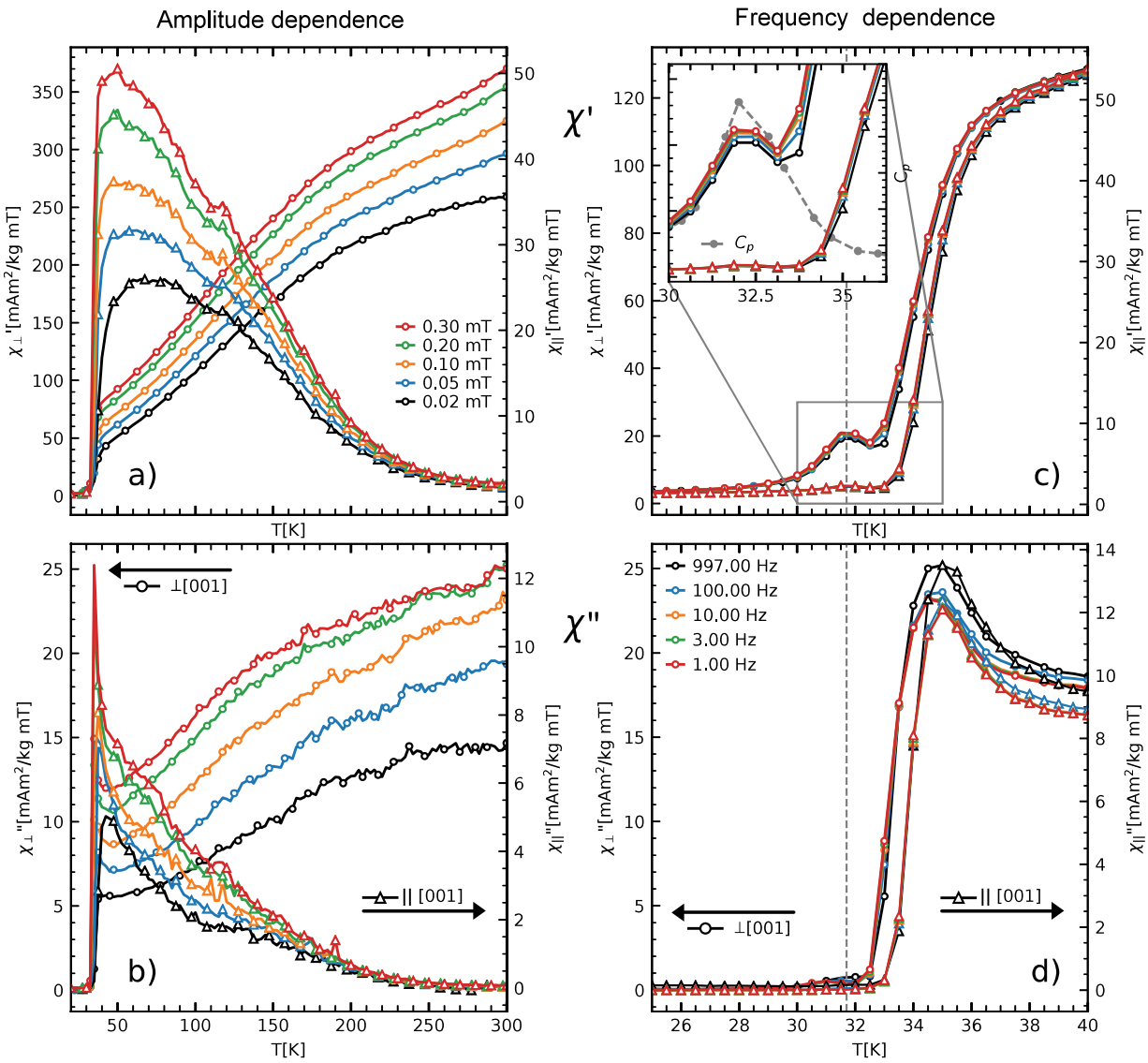

FIGURE 7. Mass-normalized in-phase (χ') and out-of-phase (χ'') susceptibility as a function of temperature in different field amplitudes (**a** and **b**) (frequency = 100 Hz, marker every fourth measurement) and frequencies (**c** and **d**) (amplitude = 0.30 mT). Circles show measurements within the basal plane ($\chi_\perp$) of the crystal, while triangles show measurements done along the crystallographic *c*-axis ($\chi_\parallel$, secondary *y*-axis). Dashed vertical lines show the maximum from the heat capacity measurement. Inset shows a zoom into the secondary peak overlaid with specific heat data (see Fig. 2) in arbitrary units. The background in specific heat was removed by polynomial interpolation.

similar changes in susceptibility for a natural Fe_7S_8 powder. They interpret the decrease in susceptibility during cooling across the Besnus transition as a reduction in domain wall mobility at lower temperatures, an explanation that would only apply to predominantly MD samples. Bezaeva et al. (2016) also reported a drop in susceptibility across the Besnus transition for predominantly single-domain 4*C* pyrrhotite, which suggests instead that something about the intrinsic magnetic anisotropy energy of the material has changed below T_{Bes}.

To gain a better understanding of how susceptibility changes at the transition, we also measured the frequency dependence of AC susceptibility ($\chi_\perp$ and $\chi_\parallel$) at high resolution (0.5 K steps) for seven frequencies (1–1000 Hz) spanning T_{Bes} (from 20–40 K). There is no frequency dependence in the in-phase data (Fig. 7c) for either $\chi_\perp$ or $\chi_\parallel$. There is a slight frequency dependence in the out-of-phase data (Figs. 7b and 7d), however, the main drop of $\chi_\parallel$ occurring at temperatures ~1 K warmer than $\chi_\perp$ in both in-phase and out-of-phase measurements. This shift is reproducible and is likely not an instrumental artifact. Furthermore, close inspection of the data of Koulialias et al. (2016) reveals a similar shift, which seems to decrease with increasing frequency.

A prominent secondary peak is visible at ~32 K (see inset in Fig. 7a) in $\chi_\perp'$ and less expressed in $\chi_\perp''$, while $\chi_\parallel$ does not show it at all. Similar features were reported by Koulialias et al. (2016) in their natural single crystal and Kind et al. (2013) in Fe_7S_8 powder. To resolve this feature, data must be collected at sufficiently high resolution (here, 0.5 K steps). Thus, the feature is not visible in the lower resolution amplitude dependence measurements (2.5 K steps). It is noteworthy that this secondary peak is located directly at the temperature of the specific heat peak discussed above. This

indicates that the peak is directly related to the transition. Consequently, a Besnus transition temperature, determined from the decay of susceptibility may be overestimating T_{Bes}.

The strong anisotropy of susceptibility in 4*C* pyrrhotite is reflected in the vastly different susceptibilities that are measured parallel and perpendicular to [001]. At room temperature, $\chi_\perp$ is ~170 times larger than $\chi_\parallel$. As temperatures approach T_{Bes}, however, $\chi_\parallel$ increases while $\chi_\perp$ decreases, which results in a linear decrease of their ratio ($\chi_\perp/\chi_\parallel$) when plotted logarithmically (Fig. 8). This linearity is broken at T_{Bes}, where the ratio shows a discontinuity, again well-aligned with the specific heat peak (see inset Fig. 7). We interpret this change a consequence of the rotation of the easy axis of the crystal during cooling. Powell et al. (2004) showed that as Fe_7S_8 is cooled, the easy axis rotates out of the (001) plane, consistent with increasing susceptibility in [001]. Similarly, the sudden increase in $\chi_\perp/\chi_\parallel$ could be caused by an abrupt rotation of the easy axis toward the basal plane and back out, toward [001].

Finally, below T_{Bes}, $\chi_\perp$ decreases to <1% of its room temperature value (Table 2); $\chi_\parallel$, on the other hand, is only reduced to about 50%. Consequently, below the transition both susceptibilities are comparable ($\chi_\perp \approx 2 \times \chi_\parallel$). Thus, the anisotropy of the crystal is greatly reduced below T_{Bes}. The sample in the study has a platelet shape, and therefore shape anisotropy may play a role. If one were to correct for the shape of our sample, the sense of the correction would lower the susceptibility within the basal plane, and therefore it is possible that susceptibility parallel to [001] could be even closer to, if not larger than, $\chi_\perp$.

Electrical resistivity

To gain an understanding of the electronic property changes that take place across the Besnus transition, we performed temperature- and magnetic-field-dependent measurements of resistivity (ρ) from 4 to 300 K, using a home-built Janis cryostat system with a 9 T superconducting magnet. Silver paste contacts were employed in a 4-wire van der Pauw configuration (van der Pauw 1958), using a Lakeshore 370 13.7 Hz AC bridge to measure 4-terminal resistances. Checks for Ohmicity, contact resistance, and self-heating were made at 4 and 300 K.

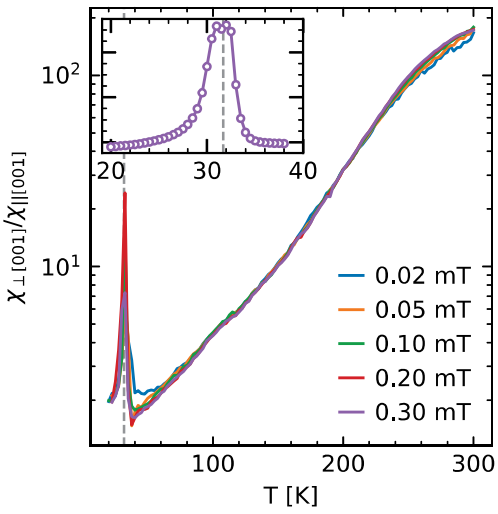

FIGURE 8. Ratios of in-plane over out-of-plane susceptibilities ($\chi_\perp/\chi_\parallel$) as a function of temperature for different field amplitudes. The inset shows the ratio determined from high-resolution AC susceptibility data (100 Hz, 0.3 mT). The dashed line shows the transition temperature determined from specific heat.

As shown in Figure 9a, the ρ in the basal plane of our 4*C* pyrrhotite single crystal exhibits clearly metallic behavior ($d\rho/dT$ is metallic-like (i.e., positive) over almost the entire temperature range, with finite apparent conductivity as $T \rightarrow 0$), with a large anomaly visible at 32 K, where the resistivity drops significantly. We note that the peak in the ratio of $\chi_\parallel/\chi_\perp$, this resistivity anomaly and the peak in specific heat are all located at the same temperature. This highlights the reproducibility and precision of T_{Bes} in our measurements, in addition to its clear, recognizable effect on diverse properties (magnetic, electronic, and thermodynamic). In contrast to the Verwey transition in magnetite, which displays a sharp drop in resistivity on warming (e.g., Kuipers and Brabers 1979), the resistivity change here is continuous, again consistent with second-order character of the Besnus transition [there is also no thermal hysteresis in $\rho(T)$ on heating/cooling]. The room temperature resistivity ($\rho_{300\,K}$) of the crystal measured here is 0.32 mΩ cm, which compares well with the $\rho_{300\,K}$ of 0.41 mΩ cm originally obtained by Besnus and Meyer (1964), being considerably lower than the 2.1 mΩ cm obtained by Charilaou et al. (2015). This consistency with the original work, and the lower values than those obtained by Charilaou et al. (2015), again highlight the quality of this phase-pure natural single crystal and reinforce the clear expression of the Besnus transition in this phase-pure sample. Consistent with this, the temperature dependence of ρ is also stronger in this crystal. For example, the residual resistivity ratio (RRR), defined as RRR = $\rho_{300\,K}/\rho_{5\,K}$, is 4.04 in this work, compared to ~2.9 in Besnus and Meyer (1964), and 1.34 in Charilaou et al. (2015). This indicates not only lower defect densities in our phase-pure crystal, but also a stronger decrease in ρ(T) below T_{Bes}. With a RRR of above 4, and also given the absolute magnitudes of the resistivities, this pyrrhotite crystal can be considered a "bad" or "dirty" metal or semimetal. In terms of constraining the *origin* of the Besnus transition, we note that any explanation for it must be able to explain a substantial *decrease* in resistivity on cooling.

Figure 9b shows the magnetic field dependence of ρ vs. T around the Besnus transition, with the field applied along a random direction in the basal plane. As the field increases from 0 to 0.5 T, progressive smearing of the sharp anomaly in ρ vs. T and a weak negative magnetoresistance (MR) is seen, meaning that the apparent T_{Bes} increases monotonically with the field, consistent with magnetization data shown in Figure 6a. In this field orientation, there is no significant additional field dependence above 0.5 T. This can be seen in the inset to Figure 9c, where the magnetoresistance {MR = $[\rho(H) - \rho(0)]/\rho(0)$} as a function of magnetic field at 32 K only shows negative MR out to ~1 T. Application of larger fields then causes an inversion in the slope of the MR and a slight increase in magnitude, saturating at high fields. The main panel of Figure 9c shows MR(9 T) as a function of temperature. Upon warming, positive MR at low temperature gives way to a slight negative MR around T_{Bes}, with the peak negative MR being about –2% at T_{Bes}. Above the transition, the MR goes positive again and remains relatively constant past 60 K at about ~0.5%. In this field orientation, MR effects are thus small, the typical growth of positive MR on cooling, as expected in a metal, being interrupted at T_{Bes} with only a small negative MR effect. This small negative

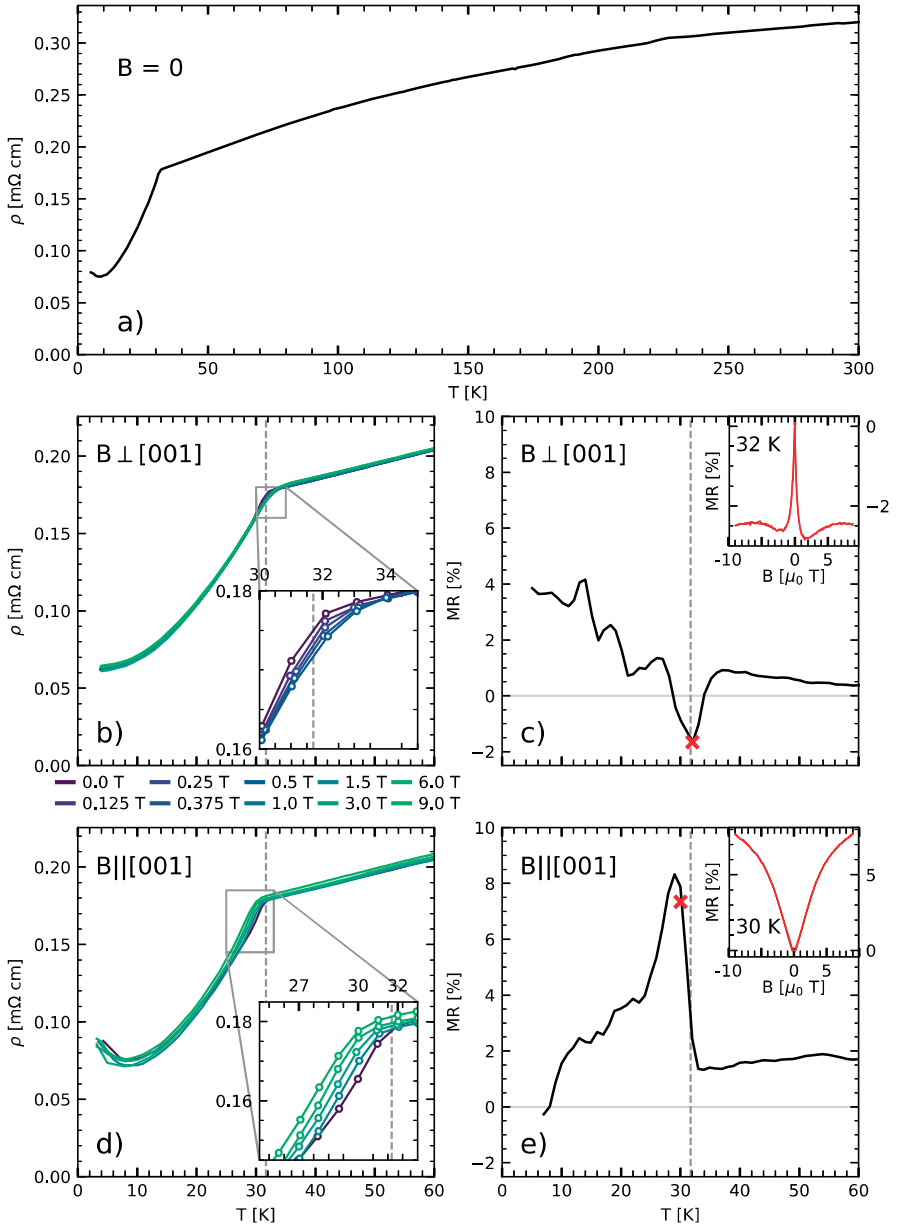

FIGURE 9. 4*C* pyrrhotite single-crystal electrical resistivity measured via the van der Pauw method as a function of temperature and magnetic field. (**a**) a-b plane resistivity (ρ) as a function of temperature (*T*) upon warming from 4 to 300 K in zero field (**b**). Panels **b**–**d** show expanded views of transport and magnetotransport properties in the T_{Bes} region. (**b**) ρ vs. *T* as a function of B (from 0–0.5 T) applied in the basal plane. (**c**) Corresponding magnetoresistance (MR) as a function of *T* at 9 T. The inset shows the B dependence of the MR at 32 K. (**d**) ρ vs. *T* as a function of B (from 0–9 T) applied along [001]. (**e**) Corresponding MR as a function of *T* at 9 T. The inset shows the B dependence of the MR at 30 K. Red crosses in **c** and **e** mark the measurement temperature for the MR(B) traces shown in the insets.

MR saturates quickly with increasing field.

Figure 9d displays the magnetic field dependence of ρ vs. *T* around the Besnus transition, this time with the field applied *out* of the basal plane, i.e., parallel to the *c*-axis. In this case, a clear decrease in the apparent transition temperature is observed as the out-of-plane magnetic field is increased from 0 to 9 T. The apparent transition temperature shift is monotonic, with an overall shift of ~2 K with 9 T of applied field, which is relatively small. The presence of an out-of-plane field thus apparently favors the $T > T_{Bes}$ phase. Importantly, this is consistent with the remanence and hysteresis data (see above) (Fig. 6c) in that when the applied field is along, or parallel to, the *c*-axis, the lowest T_{Bes} values are observed. Specifically, it appears that fields applied parallel to the *c*-axis pull the spins out-of-plane near the transition, which allows the phase above the transition to persist to lower *T*. One way to rationalize this is in terms of Zeeman energy stabilization. The $T > T_{Bes}$ phase has a larger component of magnetization along the *c*-axis than the $T < T_{Bes}$ phase [see Charilaou et al. (2015)], allowing the $T > T_{Bes}$ phase to be stabilized when a field is applied along the *c*-axis, lowering T_{Bes} as larger fields are applied. Naturally, and as shown in the expanded view in Figure 9d, the lowering of the apparent transition temperature with out-of-plane field combines

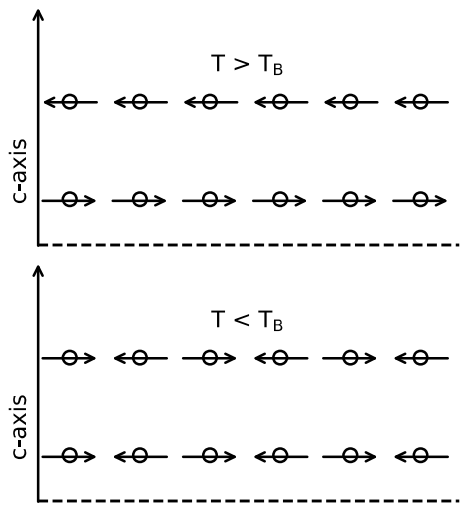

FIGURE 10. Schematic representation of exchange inversion. Arrows indicate the spins of the atoms.

with the positive $d\rho/dT$ to generate positive MR. This is shown as a function of magnetic field at 30 K in the inset to Figure 9e, where positive MR up to 7.5% is seen, not saturating even at 9 T. Figure 9e shows that this positive MR is found at all temperatures between 5–60 K when the field is applied parallel to the *c*-axis. The positive MR effect associated with the Besnus transition turns on near T_{Bes}, reaches a sharp peak, and then gradually decreases toward 5 K.

DISCUSSION

This study represents one of the most exhaustive studies of the Besnus transition to date, performed on a high-purity, phase-pure, 4*C* pyrrhotite single-crystal specimen. While the precise mechanism(s) driving the transition still remain elusive, it is possible to now better constrain potential explanations by considering all of the phenomena that have been observed to accompany the transition. Ultimately, a comprehensive theory for the Besnus transition must explain the following. (1) An entropy change at T_{Bes} resulting from an apparently second-order phase transition in specific heat (this study, Grønvold et al. 1959). (2) Loss of remanent magnetization upon cooling (RTSIRM) and warming (LTSIRM) through the transition. (3) Changing rock magnetic properties (B_c, B_{cr}, M_{rs}), while M_s remains constant. (4) Irreversible changes after cycling through T_{Bes}, represented as increases in remanence and MDF (this study, Dekkers et al. 1989). (5) The disappearance of the second inflection phenomenon in hysteresis loops at T_{Bes} (appears at ~200 K, aligned with crystal structure) (Volk et al. 2016; Koulialias et al. 2016). (6) Symmetry changes of rock magnetic properties from sixfold above the transition to fourfold below the transition (Wolfers et al. 2011; Volk et al. 2016; Koulialias et al. 2018). (7) Field dependence of T_{Bes} $\perp$[001], as determined by magnetic data and resistivity. (8) Field dependence of T_{Bes} in resistivity ||[001]. (9) Different magnetoresistive behavior when applied fields are within the basal plane or parallel to the *c*-axis. (10) A distinct decrease in resistivity on cooling through T_{Bes}. (11) Splitting of Fe sites (4 unique → 5 unique) below T_{Bes}, as determined by Mössbauer spectroscopy (Jeandey et al. 1991; Oddou et al. 1992). (12) The anomaly seen in short-range magnetic scattering seen in SANS data.

Unfortunately, no single mechanism appears capable of simply explaining all of the observed behaviors across the transition, although existing observations do allow us to rule out some proposed mechanisms, which ultimately helps constrain the nature of the transition. All of the mechanisms proposed thus far are discussed in turn below in addition to several new ones.

The role of interacting superstructures

The specimen studied here is purely 4*C* pyrrhotite and contains *no additional superstructures*, as supported by powder X-ray diffraction, microprobe analysis, heat capacity measurements, a single magnetic ordering temperature, the absence of a magnetic λ-transition, the M_s value, and the RRR value. Nevertheless, we clearly observe the Besnus transition in all physical properties studied. The specific heat shows a clear peak at ~31.7 K, in agreement with the transition temperature determined from resistivity measurements to within one kelvin at zero field. This agrees well with that of the synthetic specimen studied by Grønvold et al. (1959). The transition temperatures in the magnetic susceptibility, RTSIRM, LTSIRM, and FC curves (~32–34 K) are slightly higher than the C_P peak, but agree well with most published data (Dekkers et al. 1989; Rochette et al. 1990; Fillion and Rochette 1988; Kind et al. 2013). On the other hand, the 26 K transitions described by Charilaou et al. (2015) and Koulialias et al. (2016) deviate markedly. Baranov et al. (2014) showed that Ti substitution can induce changes in vacancy ordering, which results in a change from 4 to 3*C* in Fe_7S_8. Consequently, it seems possible that the 0.5% Ni substitution in their sample may be responsible for the additional 5*C** structure, and may explain the shifted transition temperature and the suppressed specific heat peak. More substantial Ni substitution results in an entirely new iron sulfide mineral smythite $(Fe,Ni)_9S_{11}$ with a trigonal structure, that is often found associated with pyrrhotite (Erd et al. 1957). We conclude that the Besnus transition is intrinsic to the 4*C* phase, and is not caused by interactions of different superstructures as proposed by Koulialias et al. (2016).

The role of twinning

Pyrrhotite is prone to the formation of stacking faults and twins when there are local perturbations in the superstructure (Bin and Pauthenet 1963). Thus, one could imagine that even subtle changes to the unit cell across the Besnus transition may induce twinning at the nanometer scale (Wolfers et al. 2011). The formation of such features could also reconfigure the distribution of dislocations, vacancies, and pinning sites for domain walls within the material. Consequently, the magnetic interactions between these twins would change, as well as the mobility of domain walls, and thus, the bulk magnetic properties would also change. Nanometer-scale twinning may explain the irreversible changes (e.g., enhanced remanence and coercivity) seen after low-temperature cycling. Twinning is also consistent with the length scale of the structural/magnetic changes observed in our high Q SANS data (Figs. 2c and 2d), but is somewhat inconsistent with the significant decrease in resistance observed below the transition. The decreasing resistivity can perhaps only be explained by a reduction in the number of twins. Furthermore, twinning is not able to explain the splitting of the occupancy of Fe sites observed in the Mössbauer data.

The orientation of twinning in other magnetic minerals, such as magnetite, can be influenced by applied fields, and if this were the case for pyrrhotite, it could explain the field dependence of the transition. Depending on the orientation of the twin boundaries, it is possible that the symmetry of the magnetic properties may change from sixfold to fourfold below the transition. As a mechanism, twinning could thus potentially explain many of the phenomena observed below the Besnus transition.

The role of crystallographic transitions

Wolfers et al. (2011) not only proposed a change in twinning schemes but a true crystallographic transition, with a lowering of the symmetry from monoclinic to triclinic. This is consistent with the changes in the symmetry of rock magnetic properties from sixfold symmetry above T_{Bes} to fourfold symmetry below T_{Bes} (Volk et al. 2016). Confusingly, however, our SANS data show a clear sixfold symmetry, even at 5 K. While this is not conclusive evidence against a crystallographic transition, it indicates that any crystallographic changes, if they occur, could be weak. It is worth reiterating in this regard that the 4*C* monoclinic superstructure at room temperature is only 0.26° different from a perfect hexagonal unit cell (Wolfers et al. 2011). Hence, any additional subtle distortions may not be easily detectable and will require further high-resolution crystallographic study.

A crystallographic change, where the monoclinic unit cell is subtly distorted to form a different, also monoclinic unit cell is another possible mechanism. Such an *isostructural* or *isomorphic* transformation would be difficult to detect with SANS. However, such a transition could explain many of the phenomena described above. The changing crystal structure could explain the second-order transition indicated by specific heat, but only if the phase transition is truly second-order, or very weakly first-order. A change in crystal structure would result in changes in the band structure of the material, which would affect electronic transport, i.e., the resistivity and MR. Therefore, the differences in electronic transport (specifically $d\rho/dT$) above and below T_{Bes} could potentially be explained. Furthermore, the newly created twins could change the domain structure and pin magnetic domain walls at twin boundaries. Consequently, the changing unit cell and rearrangement of domains would lead to a loss of the remanent magnetization. Pinning of domain walls, on the other hand, would increase the coercivity of the crystal. If the changes are small enough, the saturation magnetization should not be affected. Finally, the generation of twins that accompanies an isostructural transformation could explain irreversible changes on cycling through the transition.

The role of changing crystalline anisotropy

Several studies have investigated the crystalline anisotropy of pyrrhotite (Mikami et al. 1959; Bin and Pauthenet 1963; Sato et al. 1964). Bin and Pauthenet (1963) showed that the crystalline anisotropy of pyrrhotite changes upon cooling. The K_4 anisotropy constant, which dominates, shows a maximum, while the K_3 constant changes sign and becomes negative at ~200 K. The changing anisotropy causes the spins to rotate out of the basal plane, which was confirmed by neutron diffraction data by Powell et al. (2004). These changes in magnetic anisotropy may be able to explain the Besnus transition. In this scenario, the magnetic easy axis switches to a different crystallographic direction. Consequently, the remanent magnetization would be lost and domain wall orientation as well as the fundamental magnetic properties would change. However, the measurements of Bin and Pauthenet (1963) were done on an obviously twinned crystal. Furthermore, the authors were not able to determine the anisotropy from measurements in the basal plane at temperatures <60 K, as the magnetic easy axis seemed to switch when a magnetic field is applied. As the second inflection in magnetic hysteresis loops appears at ~180 K, it is likely related to this presumed easy axis switching.

On balance, it seems unlikely that the Besnus transition is solely caused by a changing anisotropy. Given that the low-temperature behavior of the crystalline anisotropy is not well known, the main changes seem to appear at 200 K. However, the remanence is unaffected, as are the magnetic properties. Furthermore, the model fails to explain the changes seen in resistivity, Mössbauer, and high-Q (Lorentzian) SANS. On the other hand, it seems likely that the anisotropy would change as a byproduct of even a subtle crystallographic transition.

The role of exchange inversion within NiAs structures

Kittel (1960) predicted a phenomenon called exchange inversion in materials with a NiAs crystal structure. Since then it has been found in Mn_2Sb and other Mn-Sb compounds with substitutions (e.g., Bither et al. 1962). At the phase transition, the formerly ferromagnetic coupling between spins switches and becomes antiferromagnetic. The spins within each Fe plane in pyrrhotite couple ferromagnetically, while the spins between layers couple antiferromagnetically. It seems possible for exchange inversion to take place at T_{Bes}. This would change the coupling within a plane to become antiferromagnetic, becoming ferromagnetic to the adjacent plane (Fig. 10). The changing spin orientation would remove most of the remanent magnetization, without affecting the bulk saturation magnetization. The field dependence of the transition could also be explained, as strong magnetic fields could exert force on the spins and hinder their reorganization. Furthermore, a reorientation of spins was found to change electronic properties in a pyrrhotite analog Fe_7Se_8 with a 4*C* NiAs structure (Li et al. 2016). While being able to explain several phenomena, this scenario fails to explain the splitting of the iron sites in Mössbauer spectroscopy. Furthermore, a spin reorganization should be visible in neutron diffraction data. Powell et al. (2004) did not observe such a transition in their neutron study. However, in their work only one scan was taken below T_{Bes}.

Future research

In light of the above, this study clearly emphasizes the need for further research along at least three lines: High-resolution structural characterization, laboratory synthesis of single-phase pyrrhotite, and linking single-crystal observations to bulk sample behavior. The observations in this study and previous work suggest that nanometer-scale twinning within pyrrhotite across the Besnus transition may explain many of the magnetic and physical properties observations. However, it is not clear which mechanism(s) may be driving the twinning. To distinguish between subtle crystallographic transitions or fundamental changes in the exchange coupling, further research is required. Wolfers et al. (2011) proposed that fine low-temperature X-ray diffraction experiments could

be used to obtain a detailed description of any crystallographic change near the 32 K transition. If such an approach is meant to differentiate between monoclinic-triclinic and isostructural transitions, then these diffraction experiments may only be possible using synchrotron facilities. Similarly, synchrotron-based X-ray absorption near-edge structure (XANES) analyses may shed light on the changes in Fe site occupancy across the transition originally observed with Mössbauer spectroscopy. Finally, powder neutron diffraction, similar to Powell et al. (2004) at temperatures spanning the transition would further show changes in spin structure as well as possible structural changes.

Magnetic methods may also help constrain the importance of twinning in mixed phase (hexagonal and monoclinic) crystals. If nanometer-scale twinning does occur across the Besnus transition, then vacancies may reorder on warming, and the distribution of pyrrhotite superstructures at room temperature may change after cycling through the Besnus transition. If so, then there should be observable changes in the nature of the λ-transition near 220 °C in susceptibility measurements. Given the field dependence of the Besnus transition observed here, it is possible that fields applied along different crystallographic directions may lead to different ratios of superstructures at room temperature. However, if no λ-transition is observed near 220 °C after cycling through the Besnus transition, then perhaps the role of twinning may need to be re-evaluated.

Implications

Many open questions remain regarding the influence of the Besnus transition on the full-vector remanence held by pyrrhotite in natural samples. While the magnitude of magnetization decreases after cycling through the Besnus transition, the direction of a laboratory-induced isothermal remanent magnetization in a single crystal of pyrrhotite is stable (Feinberg et al. 2015). This observation may have important implications for paleomagnetic studies of terrestrial and meteoritic samples containing pyrrhotite. Similar to the ways in which low-temperature treatments that cycle through the Verwey transition in magnetite are used to reduce the remanence held by large multidomain grains and give a more unfettered view of the remanence held by well-behaved, single-domain-like grains, cycling through the Besnus transition may be useful isolating high coercivity remanence in pyrrhotite. Single-domain-like grains also express a Besnus transition, but no observations exist regarding the directional stability of their magnetization across the transition.

The high purity of the 4*C* single-crystal sample in this study is particularly unusual but was essential for demonstrating the intrinsic nature of the Besnus transition and its directional dependence. However, this sample is limited in mass, and, given the numerous ongoing questions about pyrrhotite, there is a clear need to develop dependable synthesis methods (metastability is often a problem) for pyrrhotite that controls the resulting superstructures. Many existing synthesis methods are time consuming, require repeated annealing steps (which only partially control the ratio of resulting superstructures), and are limited to only producing fine-grained samples. Methods capable of producing large single crystals of well-characterized pyrrhotite would be especially beneficial to future research.

In addition, due to our improved ability to detect pyrrhotite in natural samples, it is becoming increasingly important to identify how this mineral influences or records numerous geophysical, environmental, and planetary science processes. Similarly, the mineral and its superstructures are important to the materials science community. A deeper understanding of the nature of the Besnus transition will only improve our interpretations regarding pyrrhotite. We hope this study makes a convincing case for the need for further research that combines high-resolution structural characterization with carefully controlled rock magnetic experiments on natural and synthetic bulk samples.

Acknowledgments

We thank Anette von der Handt for acquiring electron microprobe data and Jeanette Voelz for help in measuring powder X-ray diffraction data. Furthermore, we thank Rupert Hochleitner and the Bavarian Mineralogical State Collection for providing the sample material and for their kind support. E.M., B.V., M.M., and C.L. acknowledge support from the DOE through the UMN Center for Quantum Materials under DE-FG02-06ER46275 and DE-SC-0016371. We acknowledge the support of the National Institute of Standards and Technology, U.S. Department of Commerce, in providing the neutron facilities used in this work; the assistance of John Barker is gratefully acknowledged in that regard. The Institute for Rock Magnetism is a U.S. National Multiuser Facility supported through the NSF-EAR Instrumentation and Sciences Program and by funding from the University of Minnesota. This is IRM publication (no. 1710).

References cited

Arnold, R.G. (1967) Range in composition and structure of 82 natural terrestrial pyrrhotites. Canadian Mineralogist, 9, 31–50.

Aubourg, C., and Pozzi, J.-P. (2010) Toward a new <250 °C pyrrhotite–magnetite geothermometer for claystones. Earth and Planetary Science Letters, 294, 47–57.

Baranov, N.V., Ibrahim, P.N.G., Selezneva, N.V., Kazantsev, V.A., Volegov, A.S., and Shishkin, D.A. (2014) Crystal structure, phase transitions and magnetic properties of pyrrhotite-type compounds $Fe_{7-x}Ti_xS_8$. Physica B: Condensed Matter, 449, 229–235.

Bertaut, E.F. (1953) Contribution à l'étude des structures lacunaires: la pyrrhotine. Acta Crystallographica, 6, 557–561.

Besnus, M.J., and Meyer, A.J. (1964) Nouvelles données expérimentales sur le magnétisme de la pyrrhotine naturelle. Proceedings of the International Conference on Magnetism, Nottingham, Institute of Physics and the Physical Society, London, 20, 507–511.

Bezaeva, N.S., Chareev, D.A., Rochette, P., Kars, M., Gattacceca, J., Feinberg, J.M., Sadykov, R.A., Kuzina, D.M., and Axenov, S.N. (2016) Magnetic characterization of non-ideal single-domain monoclinic pyrrhotite and its demagnetization under hydrostatic pressure up to 2 GPa with implications for impact demagnetization. Physics of the Earth and Planetary Interiors, 257, 79–90.

Bin, M., and Pauthenet, R. (1963) Magnetic anisotropy in pyrrhotite. Journal of Applied Physics, 34, 1161–1162.

Bither, T.A., Walter, P.H.L., Cloud, W.H., Swoboda, T.J., and Bierstedt, P.E. (1962) New modified Mn_2Sb compositions showing exchange inversion. Journal of Applied Physics, 33, 1346–1347.

Cantu, J., Gonzalez, L.E., Goodship, J., Contreras, M., Joseph, M., Garza, C., Eubanks, T.M., and Parsons, J.G. (2016) Removal of arsenic from water using synthetic Fe_7S_8 nanoparticles. Chemical Engineering Journal, 290, 428–437.

Charilaou, M., Kind, J., Koulialias, D., Weidler, P.G., Mensing, C., Loffler, J.F., and Gehring, A.U. (2015) Magneto-electronic coupling in modulated defect-structures of natural $Fe_{1-x}S$. Journal of Applied Physics, 118, 083903-6.

Dekkers, M.J., Mattéi, J.-L., Fillion, G., and Rochette, P. (1989) Grain-size dependence of the magnetic behavior of pyrrhotite during its low-temperature transition at 34 K. Geophysical Research Letters, 16, 855–858.

Dunlop, D.J., and Özdemir, Ö. (1997) Rock Magnetism. Cambridge University Press, U.K.

Erd, R.C., Evans, H.T., and Richter, D.H. (1957) Smythite, a new iron sulfide, and associated pyrrhotite from Indiana. American Mineralogist, 42, 309–333.

Ericsson, T., Amcoff, Ö., and Nordblad, P. (1994) Vacancy ordering in Fe_7Se_8-Fe_7S_8 solid solutions studied by Mössbauer, X-ray and magnetization techniques. Hyperfine Interactions, 90, 515–520.

Fegley, B. Jr., Lodders, K., Treiman, A.H., and Klingelhöfer, G. (1995) The rate of pyrite decomposition on the surface of Venus. Icarus, 115, 159–180.

Feinberg, J.M., Solheid, P.A., Swanson-Hysell, N.L., Jackson, M.J., and Bowles, J.A. (2015) Full vector low-temperature magnetic measurements of geologic materials. Geochemistry, Geophysics, Geosystems, 16, 301–314.

Fillion, G., and Rochette, P. (1988) The low temperature transition in monoclinic pyrrhotite. Le Journal de Physique Colloques, 49, C8-907–C8-908.

Gilder, S.A., Egli, R., Hochleitner, R., Roud, S.C., Volk, M.W.R., Le Goff, M., and de Wit, M. (2011) Anatomy of a pressure-induced, ferromagnetic-to-paramagnetic transition in pyrrhotite: Implications for the formation pressure of diamonds. Journal of Geophysical Research: Solid Earth, 116, B10101.

Gillard, T.M., Phelan, D., Leighton, C., and Bates, F.S. (2015) Determination of the lamellae-to-disorder heat of transition in a short diblock copolymer by relaxation calorimetry. Macromolecules, 48, 4733–4741.
Gopal, E.S.R. (1966) Specific Heats at Low Temperatures. Plenum Press, New York.
Grønvold, F., Westrum, E.F., and Chou, C. (1959) Heat capacities and thermodynamic properties of the pyrrhotites FeS and $Fe_{0.877}S$ from 5 to 350°K. The Journal of Chemical Physics, 30, 528–531.
Grønvold, F., Stølen, S., Labban, A.K., and Westrum, E.F. (1991) Thermodynamics of iron sulfides I. Heat capacity and thermodynamic properties of Fe_9S_{10} at temperatures from 5 K to 740 K. The Journal of Chemical Thermodynamics, 23, 261–272.
Herndon, J.M., Rowe, M.W., Larson, E.E., and Watson, D.E. (1975) Origin of magnetite and pyrrhotite in carbonaceous chondrites. Nature, 253, 516–518.
Jeandey, C., Oddou, J.L., Mattéi, J.-L., and Fillion, G. (1991) Mössbauer investigation of the pyrrhotite at low temperature. Solid State Communications, 78, 195–198.
Kasama, T., Church, N.S., Feinberg, J.M., Dunin-Borkowski, R.E., and Harrison, R.J. (2010) Direct observation of ferrimagnetic/ferroelastic domain interactions in magnetite below the Verwey transition. Earth and Planetary Science Letters, 297, 10–17.
Kind, J., Garcia-Rubio, I., Charilaou, M., Nowaczyk, N.R., Loffler, J.F., and Gehring, A.U. (2013) Domain-wall dynamics in 4*C* pyrrhotite at low temperature. Geophysical Journal International, 195, 192–199.
Kittel, C. (1960) Model of exchange-inversion magnetization. Physical Review, 120, 335–342.
Kobayashi, H., Nozue, T., Matsumura, T., Suzuki, T., and Kamimura, T. (1999) The low-temperature specific heat of FeS and $M_{0.875}X$ (M = Fe, Co; X = S, Se) with a NiAs-like structure. Journal of Physics: Condensed Matter, 11, 8673–8679.
Koulialias, D., Kind, J., Charilaou, M., Weidler, P.G., Loffler, J.F., and Gehring, A.U. (2016) Variable defect structures cause the magnetic low-temperature transition in natural monoclinic pyrrhotite. Geophysical Journal International, 204, 961–967.
Koulialias, D., Charilaou, M., Schäublin, R., Mensing, C., Weidler, P.G., Loffler, J.F., and Gehring, A.U. (2018) Ordered defects in $Fe_{1-x}S$ generate additional magnetic anisotropy symmetries. Journal of Applied Physics, 123, 033902.
Kuipers, A.J.M., and Brabers, V.A.M. (1979) Electrical transport in magnetite near the Verwey transition. Physical Review B, 20, 594–600.
Lapakko, K.A. (2015) Preoperational assessment of solute release from waste rock at proposed mining operations. Applied Geochemistry, 57, 106–124.
Lashley, J.C., Hundley, M.F., Migliori, A., Sarrao, J.L., Pagliuso, P.G., Darling, T.W., Jaime, M., Cooley, J.C., Hults, W.L., Morales, L., and others. (2003) Critical examination of heat capacity measurements made on a quantum design physical property measurement system. Cryogenics, 43, 369–378.
Levinson, L.M., and Treves, D. (1968) Mössbauer study of the magnetic structure of Fe_7S_8. Journal of Physics and Chemistry of Solids.
Li, C.H. (1932) Magnetic properties of magnetite crystals at low temperature. Physical Review, 40, 1002–1012.
Li, G., Zhang, B., Baluyan, T., Rao, J., Wu, J., Novakova, A.A., Rudolf, P., Blake, G.R., de Groot, R.A., and Palstra, T.T.M. (2016) Metal–insulator transition induced by spin reorientation in Fe_7Se_8 grain boundaries. Inorganic Chemistry, 55, 12912–12922.
Mikami, I., Hirone, T., Watanabe, H., Maeda, S., Adachi, K., and Yamada, M. (1959) On the magnetic anisotropy of a pyrrhotite crystal. Journal of the Physical Society of Japan, 14, 1568–1572.
Morimoto, N., Nakazawa, H., Nishigucmi, K., and Tokonami, M. (1970) Pyrrhotites: Stoichiometric compounds with composition $Fe_{n-1}S_n$ ($n \geq 8$). Science, 168, 964–966.
Muttoni, G. (1995) "Wasp-waisted" hysteresis loops from a pyrrhotite and magnetite-bearing remagnetized Triassic limestone. Geophysical Research Letters, 22, 3167–3170.
Muxworthy, A.R., Bland, P.A., Davison, T.M., Moore, J., Collins, G.S., and Ciesla, F.J. (2017) Evidence for an impact-induced magnetic fabric in Allende, and exogenous alternatives to the core dynamo theory for Allende magnetization. Meteoritics & Planetary Science, 112.
Nakazawa, H., and Morimoto, N. (1970) Pyrrhotite phase relations below 320°C. Proceedings of the Japan Academy, 46, 678–683.
Oddou, J.L., Jeandey, C., Mattéi, J.-L., and Fillion, G. (1992) Mössbauer study of the low-temperature transition in pyrrhotite. Journal of Magnetism and Magnetic Materials, 104-107, 1987–1988.
O'Reilly, W., Hoffmann, V., Chouker, A.C., Soffel, H.C., and Menyeh, A. (2000) Magnetic properties of synthetic analogues of pyrrhotite ore in the grain size range 1-24 μm. Geophysical Journal International, 142, 669–683.
Pastor, J.M., Pérez-Landazábal, J.I., Gómez-Polo, C., Recarte, V., Larumbe, S., Santamarta, R., Fernandes Silva, M., Gómez Pineda, E.A., Winkler Hechenleitner, A.A., and Lima, M.K. (2012) Entropy change linked to the magnetic field induced Morin transition in Hematite nanoparticles. Applied Physics Letters, 100, 063102.
Powell, A.V., Vaqueiro, P., Knight, K.S., and Chapon, L.C. (2004) Structure and magnetism in synthetic pyrrhotite Fe_7S_8: A powder neutron-diffraction study. Physical Review B, 70, 014415.
Quidelleur, X., Valet, J.-P., and Thouveny, N. (1992) Multicomponent magnetization in paleomagnetic records of reversals from continental sediments in Bolivia. Earth and Planetary Science Letters, 111, 23–39.
Rochette, P., Fillion, G., and Dekkers, M.J. (2011) Interpretation of low-temperature data Part IV: The low-temperature magnetic transition of monoclinic pyrrhotite. The IRM Quarterly, 21, 1–11.
Rochette, P., Fillion, G., Mattéi, J.-L., and Dekkers, M.J. (1990) Magnetic transition at 30–34 Kelvin in pyrrhotite: insight into a widespread occurrence of this mineral in rocks. Earth and Planetary Science Letters, 98, 319–328.
Rochette, P., Lorand, J.P., Fillion, G., and Sautter, V. (2001) Pyrrhotite and the remanent magnetization of SNC meteorites: a changing perspective on martian magnetism. Earth and Planetary Science Letters, 190, 1–12.
Rosenberg, H.M. (1963) Low Temperature Solid State Physics. Oxford University Press, New York.
Sato, K., Yamada, M., and Hirone, T. (1964) Megnetocrystalline anisotropy of pyrrhotite. Journal of the Physical Scociety of Japan, 19, 1592–1595.
Schwarz, E.J., and Vaughan, D.J. (1972) Magnetic phase relations of pyrrhotite. Journal of Geomagnetism and Geoelectricity, 24, 441–458.
Sharp, W.E. (1966) Pyrrhotite: a common inclusion in south african diamonds. Nature, 211, 402–403.
Shepherd, J.P., Koenitzer, J.W., Aragón, R., Spalek, J., and Honig, J.M. (1991) Heat capacity and entropy of nonstoichiometric magnetite $Fe_{3(1-\delta)}O_4$: The thermodynamic nature of the Verwey transition. Physical Review B, 43, 8461–8471.
Shimada, K., Mizokawa, T., Mamiya, K., Saitoh, T., Fujimori, A., Ono, K., Kakizaki, A., Ishii, T., Shirai, M., and Kamimura, T. (1998) Spin-integrated and spin-resolved photoemission study of Fe chalcogenides. Physical Review B, 57, 8845–8853.
Shirai, M., Suzuki, N., and Motizuki, K. (1996) Electronic band structure and photoemission spectra of Fe_7S_8. Journal of Electron Spectroscopy and Related Phenomena, 78, 95–98.
Tokonami, M., Nishiguchi, K., and Morimoto, N. (1972) Crystal structure of a monoclinic pyrrhotite (Fe_7S_8). American Mineralogist, 57, 1066–1080.
van der Pauw, L.J. (1958) A method of measuring the resistivity and Hall coefficient on lamellae of arbitrary shape. Phillps Technical Review, 20, 220.
Volk, M.W.R., Gilder, S.A., and Feinberg, J.M. (2016) Low-temperature magnetic properties of monoclinic pyrrhotite with particular relevance to the Besnus transition. Geophysical Journal International, 207, 1783–1795.
Weiss, B.P., Maloof, A.C., Tailby, N., Ramezani, J., Fu, R.R., Hanus, V., Trail, D., Bruce Watson, E., Harrison, T.M., Bowring, S.A., and others. (2015) Pervasive remagnetization of detrital zircon host rocks in the Jack Hills, Western Australia and implications for records of the early geodynamo. Earth and Planetary Science Letters, 430, 115–128.
Wolfers, P., Fillion, G., Ouladdiaf, B., Ballou, R., and Rochette, P. (2011) The pyrrhotite 32 K magnetic transition. Solid State Phenomena, 170, 174–179.
Zhang, Kailong, Zhang, T., Liang, J., Zhu, Y., Lin, N., and Qian, Y. (2015) A potential pyrrhotite (Fe_7S_8) anode material for lithium storage. RSC Advances, 5, 14828–14831.
Zhang, Ke, Zheng, H., Wang, J., and Wang, R. (2008) Transmission electron microscopy on iron monosulfide varieties from the Suizhou meteorite. Physics and Chemistry of Minerals, 35, 425–432.

Manuscript received February 16, 2018
Manuscript accepted June 11, 2018
Manuscript handled by Sarah Brownlee

Endnotes:

[1]Deposit item AM-18-106514, Supplemental Figure. Deposit items are free to all readers and found on the MSA web site, via the specific issue's Table of Contents (go to http://www.minsocam.org/MSA/AmMin/TOC/2018/Oct2018_data/Oct2018_data.html).

[2]Muhlbauer, S., Honecker, D., Perigo, E., Bergner, F., Disch, S., Heinemann, A., Erokhin, S., Berkov, D., Leighton, C., Eskildsen, M., and others , Magnetic small-angle neutron scattering. Reviews of Modern Physics, in review.